Unlocking the Past: A review of digital processing of historical aerial and satellite stereo analog imagery for geoscience applications

Livia Piermattei, Robert Mcnabb, Melanie Elias, Camillo Ressl, Amaury Dehecq, Luc Girod, Thomas Dewez, Anette Eltner

GRSM-2025-00058

Unlocking the Past: A Review of Historical Aerial and Satellite Stereo-Imagery for Geoscience Applications

Livia Piermattei, Robert McNabb, Melanie Elias, Camillo Ressl, Amaury Dehecq, Luc Girod, Thomas Dewez, Anette Eltner

***Abstract*—Dramatic changes have occurred over the past century in many parts of the planet due to natural factors and intensifying human activities. Understanding these changes is critical for quantifying long-term environmental trends and modelling future conditions. A vast, underexploited resource for such analysis lies in historical aerial and satellite stereo imagery captured with analogue cameras from the early 1900s to the early 2000s. Originally acquired for military and mapping purposes, the stereoscopic nature of historical images offers a unique potential to reconstruct 3D Earth surface changes across the 20th century. Recent algorithmic advances in photogrammetry and computer vision have greatly enhanced this potential. Despite the early recognition of their value, these datasets remain underexploited due to challenges related to 1) fragmented and inaccessible archives, 2) digitisation and associated costs, and 3) a lack of scalable, automated processing solutions. This review addresses these challenges by analysing 198 studies that digitally process historical aerial and satellite stereo imagery for orthoimage and DEM generation. We provide an overview of accessed archives, processing strategies, and software pipelines. We discuss emerging tools and advances in image-matching algorithms and georeferencing solutions and highlight how historical imagery can support a wide range of geoscientific applications, from climate change to urban development. Finally, we emphasise the urgent need to unlock these archives and develop efficient, reproducible workflows to preserve and exploit this irreplaceable remote sensing dataset before physical degradation or institutional neglect make it inaccessible.**

***Index Terms*—Historical aerial and spy satellite stereo images, Analogue film cameras, Historical image archive, Digital photogrammetry, Digital elevation model, 20th century environmental changes.**

I. Introduction: The untapped value of historical stereo imagery

Historical or archival photographs captured with analogue cameras, using film or glass plates, have long been utilised in environmental applications and geoscientific research. Terrestrial photographs, whether monoscopic images (from single stations) or stereo pairs, were acquired worldwide for topographic mapping and land surveying for both civilian and military purposes until the early 1950s. The systematic use of aerial photography began in the 1930s in North America and Europe, with countrywide coverage organised by military or governmental mapping agencies between the World Wars. After World War II, aerial photography expanded globally into non-military and research fields, such as landscape studies, geological mapping, archaeology, and broader environmental sciences. By the 1960s, high-resolution film cameras were also deployed on U.S. and soviet reconnaissance satellites to observe areas of geopolitical interest [1]. Similar technologies were later used by Soviet commercial satellites in the 1970s, continuing until the early 2000s.

As a result of nearly a century of analogue camera acquisition, millions of aerial and satellite photographs have been collected worldwide. These photographs capture the state of the environment at the time they were taken [2], documenting the evolution of land cover and topography over the past century. Their scientific value lies not only in their age, worldwide coverage, and high spatial resolution but mainly in their stereoscopic acquisition, i.e., the same area is seen in two images captured from different perspectives. This acquisition method enables the reconstruction of a two-dimensional (2D) orthoimage and a three-dimensional (3D) digital elevation

This work was partially supported by the BRGM seed fund project "M4 MNS Historiques", the "RenovRisk-Erosion" project jointly funded by Reunion Island's Regional Council, and in part by the Glacier4D (DFG grant number 436500674), the European Union (FEDER), the French Government and BRGM and the SEHAG project ("Sensitivity of High Alpine Geosystems to Climate Change Since 1850"), financially supported by the German Research Foundation (DFG, project ER 905/1-1, project no. 409552118) and the Austrian Science Fund (FWF) (grant numbers: BE 1118/38-1, BE 1118/39-1, BE 1118/40-1, HA 5740/10-1, HE 5747/6-1, ER 905/1-1, DI 639/5-1, CH 981/3-1, MA 6966/4-1, LA 4426/1-1 and 4062-N29). *(Corresponding author: Livia Piermattei).*

Livia Piermattei is with the Department of Geography, University of Zurich, 8057 Zurich, Switzerland (email: livia.piermattei@geo.uzh.ch). Robert McNabb is with the School of Geography and Environmental Sciences, Ulster University, BT52 1SA Coleraine, UK (email: r.mcnabb@ulster.ac.uk). The authors Melanie Elias and Anette Eltner are with the Institute of Photogrammetry and Remote Sensing, TUD Dresden University of Technology, 01069 Dresden, Germany (email: melanie.elias@tu-dresden.de, anette.eltner@tu-dresden.de). Camillo Ressl is with TU Wien, Department of Geodesy and Geoinformation, Vienna, 1040, Austria (email: camillo.ressl@geo.tuwien.ac.at). Amaury Dehecq is with the Université Grenoble Alpes, IRD, CNRS, Grenoble INP, INRAE, Institut des Géosciences de l'Environnement (IGE), 38000 Grenoble, France (email: amaury.dehecq@univ-grenoble-alpes.fr). Luc Girod is with the Department of Geosciences, University of Oslo, 0371 Oslo, Norway (email: luc.girod@geo.uio.no). Thomas Dewez is with BRGM, Direction of Risks and Mitigation, F-45060 Orléans, France (email: t.dewez@brgm.fr).

This article has supplementary downloadable material available at [link], provided by the authors.

model (DEM) [3] using photogrammetry, i.e., the science and technology of deriving 2D and 3D information of an object through photographs.

The usage of historical imagery in geosciences can be broadly grouped into three categories: (1) communication and education through repeat photography, often used to visually document land cover change [4]; (2) mapping, where orthophotos often serve as the primary documentation source (e.g., [5], [6]); and (3) surface change detection, both horizontally and in elevation. For change detection research, historical aerial images provide the longest-available, temporally continuous, and spatially complete records of landscape change [7]. In countries with extensive historical aerial image archives and repeat acquisitions at intervals of 4–10 years [8], researchers can conduct detailed multi-temporal analyses of geomorphic processes. Fig. 1 illustrates one such application in a proglacial alpine catchment. When combined with modern digital remote sensing data, aerial and satellite historical stereo images remain the only remote sensing source for quantifying long-term 3D surface changes at high spatial resolutions across local to global scales, providing valuable data for environmental research and climate change studies [9], including calibration data for modelling surface processes under future climate scenarios. Another unique historical dataset for 3D reconstruction is terrestrial historical image archives, although the stereoscopic acquisition is very rare [10]. Overviews of the applications of aerial and U.S. spy satellite images are provided by [11] and [12], respectively.

The early recognition of the immense value of these historical photographs [13], [14] is demonstrated by the efforts to recover, preserve, and digitise photographic archives and distribute the scanned images to the public via online platforms. However, the full exploitation of these data has long been hindered by the technical complexity of photogrammetric processing. Traditional analogue processing required expensive equipment and specialised expertise [15], and even early digital desktop photogrammetry, available from the late 1980s, was cumbersome and inaccessible to non-experts. A significant change occurred in the past decade with the implementation of Structure from Motion (SfM; [16]) and computer vision algorithms in user-friendly, low-cost software and tools. Although these tools were initially developed for digital images (e.g., [17]), the scientific community soon applied them to historical archives, enabling the 3D surface reconstruction of multiple overlapping scanned historical images (e.g., [18]).

Despite these technological advancements and increased research in (re)processing historical images [8], several challenges still limit their widespread use [19]. Key challenges are related to 1) fragmentation and inaccessibility of archives, 2) digitisation and costs, and 3) a lack of automated and scalable processing solutions [20], [21].

Millions of aerial photographs worldwide are stored across regional, national, military, and private collections [22], [23]. The absence of a geo-catalogue and inconsistent metadata for many of these archives makes it difficult to assess the extent of available data. Yet, a comprehensive global inventory of these archives, particularly for aerial images, including information on temporal and spatial coverage and stereo capability, is lacking. Furthermore, the quality of these images is often degraded by film ageing, poor physical storage, and low-quality scanning [11], [21], [24], [25]. Only a fraction of these images have been digitised, and the high cost of scanning and purchasing previously digitised historical images continues to pose a considerable financial barrier for large-scale research. Even where images are scanned, heterogeneity in camera types, flight configurations, and the frequent absence of metadata (e.g., camera calibration protocols, fiducial marks, and ground control points) complicates automated photogrammetric processing [2]. There is also a lack of clear workflows tailored specifically to historical stereo images, as photogrammetric software has only marginally reached the non-specialist community. Until recently, SfM tools have not been designed to handle scanned images, and the application of artificial intelligence and deep learning algorithms to historical imagery is still emerging.

To address these challenges and increase awareness, accessibility, and usability of scanned stereo aerial and satellite images from analogue cameras (hereafter referred to as historical images), we systematically reviewed studies that processed historical images. We screened over 400 publications (as of 2024), ultimately selecting 198 peer-reviewed studies that met our criteria: studies that processed historical stereo aerial or satellite imagery into DEM or orthoimages using digital photogrammetry. Studies that employed analytical photogrammetry, used terrestrial imagery only, used monoplotting techniques, performed image rectification, relied on preexisting historical orthophotos or DEMs, or lacked image processing information are not the focus of our review. From the selected subset, we built a publicly available relational database that captured information on study areas, applications, image archives, camera specifications, metadata, datasets, processing methods, software used, and the resulting outputs and accuracy assessments (Figure A.4, Table A.1).

This method-focused meta-analysis review identifies key trends in the digital photogrammetric processing of historical images. It offers practical insights into the archives accessed by the reviewed studies, challenges, processing techniques and emerging tools and workflows. We also identify several critical barriers that continue to limit the broader use of historical imagery. Finally, we argue for urgent action to digitise and unlock historical image archives, develop reproducible and adaptable workflows that accommodate different cameras with varying metadata, and standardise the reporting of dataset information and accuracy metrics. These actions will help preserve this invaluable remote sensing resource and ensure it can be leveraged before it is degraded or lost.

II. Challenges of historical aerial and satellite images

Processing historical aerial and satellite images captured with analogue film or plate cameras presents several challenges, particularly when performing automated or multi-temporal photogrammetric workflows, as outlined in Table 1. Early studies [26], [27] highlighted difficulties in matching features

across image sequences due to surface changes between acquisition dates. These challenges are further intensified by radiometric inconsistencies in 8-bit black-and-white imagery, especially in complex environments such as forests [28], large water bodies [29], [30], and ice- or cloud-covered surfaces [31]. Photographs are rarely available as original negatives or image diapositives, and scans from paper contact prints are subject to significant non-uniform geometric distortions, especially when desktop scanners are used [32]. Furthermore, inconsistent digitisation protocols across epochs can complicate inter-temporal comparisons [21]. Long-term storage under poor conditions, such as excessive heat and humidity, can also cause irreversible physical and chemical degradation of film, negatives, and paper prints, leading to issues such as dilation or contraction, changes in chemical state, and reduced photo contrast [33].

Early aerial reconnaissance photographs, often acquired with a non-metric camera, do not exceed 30-60% image overlap ([34]; cf. Fig. 2b). The lack of metadata, calibration protocols, and the large variability in acquisition methods (e.g., nadir, oblique, panoramic), formats, and fiducial mark types (Fig. 2c) further limit the reproducibility and transferability of photogrammetric processing workflows [34], [35], [36], [37].

Spy satellite images face additional challenges, such as image size and distortion [38]. Corona satellite images are known to contain significant deformations compared to conventional frame cameras [38], [39], [40], [41], [42] due to the panoramic geometry used to capture large swaths and acquisition characteristics (Fig. 3b), such as the cylindrically shaped film mounting device and the Image Motion Compensation device [43]. Distortions are primarily conical distortion and S-shaped deformation caused by the movement of the satellite during film exposure through a rotating wheel; these effects are more pronounced at the image edges along the satellite track [38], [40], [44]. Furthermore, scanning spy satellite images can be complex due to the large film size; for example, Corona images measure 7 cm by 75.7 cm, and the KH-9 panoramic film can reach up to 319.4 cm in length, depending on the scan angle. This size exceeds the format size of any photogrammetric scanner. Thus, photographs are often scanned in multiple parts that overlap to ensure no information is lost and enable the merging of the sub-images. This complex scanning process often introduces alignment errors and visible artefacts in the resulting DEMs [24], [25].

Finally, the large size of high-resolution scans presents practical challenges for data handling. A single grayscale aerial image scanned at 1200 dpi (21.16 µm) can reach ~250 MB, while Corona panoramic and Hexagon mapping frame images can exceed 1.2 GB and 2.5 GB, respectively.

III. Historical image archives

To fully understand the amount and diversity of historical aerial datasets, including the areas surveyed and the variety of image formats, one must consider the evolution of aerial photography, from its early military purposes to the development of camera systems and processing techniques (see Supplement A1). Millions of stereo aerial images have been acquired globally, mainly since World War I, and not all of these images have survived [45] or are accessible [46]. Aerial photograph archives were already in place when the images were first acquired. As a single negative could produce multiple prints, images were often dispersed to different locations. Consequently, historical aerial images are spread (sometimes with duplicates) across global, regional, and national collections, as well as small local or specialised collections [22]. An overview of the current state of archiving and geoprocessing of historical aerial images in Europe was attempted by [8] and, more recently, by [11], with a focus on Polish archives. However, a comprehensive list of archives worldwide, along with information on the temporal and spatial coverage and stereo capability of the historical images, is currently missing.

The world's two most extensive collections of aerial photographs are the National Collection of Aerial Photography (NCAP; formerly known as The Aerial Reconnaissance Archives, TARA) and the US National Archives and Records Administration (NARA) [47]. NCAP preserves millions of military intelligence images from World War II to the 1980s [22], [45], which are accessible both online and in person [48]. NARA's Cartographic Branch holds over 35 million aerial photos dating from 1918 to 2011, from US and allied forces, along with 1.2 million German and Japanese reconnaissance prints, and declassified U-2 images [49].

At the national level, nearly all countries maintain archives of aerial photographs [22], often managed by military or mapping agencies. The worldwide distribution of the image archives is demonstrated by the geographic spread of the research sites (or photographed areas) that process and utilise historical imagery (Fig. 4). A significant portion of global coverage is derived from declassified US spy satellites, particularly in Arctic regions and High-mountain Asia (Fig. 4b). Most aerial image studies are concentrated in Europe and US (Fig. 4a), sourced from national aerial archives, but also include work in Japan [50], Australia [51], Canada [52], Antarctic [53] and the Arctic [54]. Images of colonial-era regions in Africa [55], [56] and Asia are frequently stored in European archives [22] (Fig. 4).

Our review identified 83 named archives across 35 countries, with the United States and the United Kingdom hosting the highest numbers at 13 and 8, respectively (Table 2). Table 2 presents a selection of aerial image archives referenced in the reviewed literature, including only those for which direct or derived online access links were available. Access policies vary considerably across archives. For example, France, Spain, Iceland, and Switzerland have provided free scanned aerial images since a few years, whereas institutions in Italy, Austria, and Australia may charge based on scan quality and resolution. However, over half of the reviewed studies did not report the archive source or access details (Fig. 5).

American and Soviet satellite images provide global coverage and often offer stereo capabilities (Fig. 6b). Supplement A2 describes the historical context of spy satellite images.

American “KeyHole” or KH satellite images were

progressively declassified by executive orders in 1995 (Corona), 2002 (Hexagon mapping camera), and 2011 (Hexagon panoramic camera) [57], [58]. Table 3 summarises the main American missions relevant to geoscience applications. Scanned images can be freely accessed via the USGS Earth Explorer portal [59], while on-demand scanning for unscanned images or a subset of duplicate film held in the USGS costs $30 per scene. Images come with crude geolocation (kilometre accuracy) of the image corners and a priori focal length information. The satellites typically carried black-and-white film, but some documentation mentions that infrared or colour film is sporadically used [57]. The global coverage and image count of the Corona and Hexagon programmes from the 1960s to 1980s are shown in Fig. 6a, based on the USGS archives. Additional detailed information on the satellite and camera systems of the Corona and Hexagon programmes can be found in [60] and [58].

Soviet-era satellite images were made commercially available through the Soyouzkarta programme [61]. Publications from the 1990s reveal that Sovinformsputnik sold images from the TK-200, TK-250, TK-350, KVR-1000 and KVR-3000 cameras [62], [63], [64], [65], while Gostsenter Priroda sold imagery from KATE-200, KFA-1000, KFA-3000 and MK-4 cameras [66], [67], [68]. Eastview and Terraserver also marketed these products. At this time, companies such as Innoter appear to sell Resurs-F images, but we could not find precise information on the access and pricing of this data. The global coverage of all available images from the Soviet/Russian missions is illustrated in Fig. 6b.

IV. Historical image datasets, products and applications

Interest in historical image processing for geoscience applications has been steadily increasing, especially since 2015 (Fig. 7), likely due to the widespread use of SfM workflows in low-cost software and the increased availability of historical images. Among the reviewed studies, aerial images have drawn more interest (139 studies) compared to satellite images (50), possibly because of their higher spatial resolution and more standardised image processing workflows compared to the different geometries of satellite data. Furthermore, spy satellite images have only recently been declassified and remain relatively unknown, although [69] developed two methods to generate DEMs from Corona images as early as 2000. The combination of aerial and satellite image datasets ("Combined" category in Fig. 7) has not yet been widely utilised, except for a few studies [70], [71], [72], [73], [74], [75], [76], [77] (Fig. 8a).

Aerial images are often used for multi-temporal analyses as multiple acquisitions typically exist for the same area, enabling the reconstruction of historical time series from different epochs (here referred to as datasets; Fig. 8a). In contrast, satellite datasets, particularly from U.S. KH missions, are generally limited to single snapshots and are often combined with modern digital sensors to extend the observation period. Overall, we identified 630 image datasets across studies, including 114 from spy satellites.

The primary motivation for accessing and processing historical images is to reconstruct 3D data, such as point clouds and DEMs, although orthophotos are also generated in various fields for mapping and image classification (Fig. 7). Glaciology and geomorphology are the main fields applying 3D reconstructions. Glaciological studies often use long time series to assess elevation changes and glacial mass loss over time (e.g., [78], [79], [80], [81], [82]), and natural hazards [83] using both aerial and satellite images. Geomorphological applications benefit significantly from the high spatial and temporal resolution of repeated aerial acquisitions (Fig. 8a), with some studies combining more than ten historical aerial datasets for proglacial studies (e.g., [3], [18], [84], [85], [86], [87], [88]). Other applications include fluvial geomorphology, topography of reservoir lakes [89], landslide monitoring (e.g., [90], [91]) and coastal dynamics (e.g., [92], [93]).

Other domains, such as archaeology, forestry, volcanology, and urban studies, appear less frequently in 3D processing workflows (Fig. 7), likely because these disciplines often rely on existing orthophoto archives, reducing the need for custom reconstruction. A growing area of research focuses on optimising processing workflows of historical images, including automated calibration, georeferencing, machine learning and accuracy assessment.

For some countries, historical aerial images date back to the 1910s and 1920s [94], but they are more widely accessible from the 1930s and 1940s onwards, up to the early 2010s (e.g., [95]). Declines in availability during World War II (Fig. 8) likely reflect restrictions on civilian flights and data loss over time. Despite several datasets having been processed worldwide, our database also emphasises the significant yet underutilised potential of historical image archives.

Out of millions of available images (e.g., aerial image counts range from 1 million in Sweden and Norway to 5 million in France and Italy, and up to 30 million images in the UK) most studies have processed only a small number of aerial and satellite images, focusing primarily on local and catchment-scale areas (Fig. 8b, 8c). Exceptions exist at national and regional scales, such as [96], covering all ice-free areas of Greenland; [97] in Switzerland, and [54] in Svalbard. The reviewed studies processed approximately 37,000 aerial images covering over 950,000 km², which represents about 1% of the Earth's land surface.

Although there is a general correlation between the size of the study area and the number of aerial images processed (Fig. 8b), the coverage also depends on factors such as flight height and viewing angle (nadir, oblique, or panorama). In contrast, satellite images cover much larger areas per image; for instance, 424 Hexagon mapping camera images processed by [24] provided near-global glacier coverage. However, the number of processed spy satellite images is also very low, considering the nearly 1.5 million images that are currently accessible for scanning and download through the USGS online repository (Fig. 6). A single pair of KH-9 mapping camera images can cover roughly 30,000 km², whereas a typical aerial image captured at an altitude of 1,000 meters with a 150 mm focal length and 23 cm x 23 cm film covers only 0.42 km².

Historical images vary in scale, format, and quality, with most being near-vertical black-and-white images [46] captured on nitrate, acetate, or polyester film [33]. Polyester film, introduced in the 1960s, proved to be more chemically stable and was adopted in missions such as the US Corona programme [98]. The focal length, flight height, and scanner resolution define the Ground Sampling Distance (GSD), the distance between two consecutive pixel centres measured on the ground. This parameter is important because it is a good approximation of the achievable resolution of the orthophoto and DEM, which is correlated to their potential accuracy. The larger the GSD value, the lower the spatial resolution of the image, resulting in less visible details. The GSD of the reviewed aerial datasets spans from 0.05 m to 7.5 m (Fig. 9a), with a few datasets up to 60 m from oblique images [70]. Some studies report GSD values below 10 cm (e.g., [99], [100], [101]), but in more than 85% of cases, the GSD falls between 0.10 m and 1 m. Image scales are also occasionally reported, ranging from 1:440 to 1:40,000. Spy satellite images generally have a coarser resolution due to the higher flight altitude of satellite platforms, with GSD values between 2 m and 8 m and scanning resolutions between 7 and 14 microns (µm) (Fig. 9b). Two studies [102], [103] used Argon spy satellite images with a 'nominal ground resolution' of 140 m, improved to 33 m through high-resolution scanning.

The geometric resolution of the orthophoto and DEM should closely match the processed GSD. As expected, orthophotos exhibit higher spatial resolution than DEMs (Fig. 10), with an average resolution approximately four times greater. On average, products derived from aerial images have a spatial resolution of 0.9 m and 3 m for the orthophoto and DEM, respectively. Satellite products tend to have coarser resolution, with an average resolution of 4.8 m for orthophotos and 23 m for DEMs, although higher resolutions can be achieved, for example, with the KH-9 Hexagon panoramic camera. These resolutions are suitable for a broad range of environmental and geoscientific applications. High-resolution products (<5 m) are especially relevant for geomorphology, forestry, and volcanology, while glaciological studies often tolerate coarser satellite-based products. Nevertheless, a direct link between application type and required resolution is not clear, as choices often reflect data availability more than precision needs.

V. Digital processing of historical stereo images in geoscience

The general photogrammetric workflow for deriving 2D and 3D information from overlapping historical images begins with image scanning, pre-processing, followed by image orientation and calibration. Once oriented, 3D point clouds are extracted to generate DEMs and orthophotos. Post-processing steps are required before accuracy assessment (Fig. 11). Each step involves multiple measurements and parameters that impact the accuracy of the final output.

This review analyses 198 studies comprising 630 datasets to evaluate how historical images are processed, including software tools, recent advances in image processing, and accuracy assessment. Additionally, it provides theoretical context and practical guidance for cases where metadata is incomplete or missing.

A. Theoretical background of image orientation and calibration

The processing of historical imagery is primarily based on two main methods: classical photogrammetry and SfM. The general workflows for both methods are illustrated in Fig. 12a and 12b, although several variants are employed according to the availability of metadata, GCPs, and the specific software and its version. The key difference between the two approaches lies in their dependency on prior knowledge of camera parameters. Classical photogrammetry typically requires approximated exterior orientation (i.e. the camera position and orientation, which defines the projection geometry in space), and interior orientation (i.e., camera calibration parameters such as focal length, location of principal point, radial lens distortion coefficients and photo coordinates of the fiducial marks). These parameters are traditionally derived from high-precision laboratory-based calibration [104] and stored in the calibration protocol/certificate of this specific laboratory camera calibration [105]. However, such metadata are frequently missing in historical aerial datasets, and those of spy satellites remain classified to this date. For aerial images from the 1940s onwards, the calibrated principal distance can also be found on the actual image as part of auxiliary data, usually along one edge of the image. An example is provided in Figure A.3 from a Fairchild aerial metric camera. Depending on the camera model, any of the following information may be visible [106]: calibrated focal length, camera (lens) serial number, photo number, flight date, absolute flying height, image scale, spirit level, and exterior orientation data (when GPS was already in use). Also, in Soviet satellite images, the calibrated focal length is printed on the film.

SfM does not require initial orientation estimates of these parameters as it uses automated tie point extraction and self-calibration techniques to estimate them. Tie points are automatically extracted in both SfM and photogrammetry approaches via image matching algorithms to provide relative orientation between overlapping images (Fig. 12). Both approaches also use Bundle Block Adjustment (BBA; [107]), a mathematical optimisation process that simultaneously refines both the interior and exterior orientation parameters across a set of overlapping images. BBA works by solving the collinearity equation, which expresses, using the mentioned orientation parameters, that the projection centre, the observed image point, and the respective object point lie on a straight line.

For scanned analogue images, an additional calibration step is necessary before exterior and interior image orientation can be performed. This pre-processing step consists of the transform of image coordinates from the (digital) scanner's pixel system into the (analogue) calibrated camera coordinate system. This is achieved by identifying fiducial marks and applying 2D similarity (four parameters: one shift in x and y each, one rotation, and one scale), affine (six parameters: shift in x and y, two rotations, one scale in x and y each), or bilinear transformations (eight parameters: shift in x and y, two

rotations, scale in x and y, one linear scale change in x and y each), depending on the number and quality of fiducial marks detected. Usually, when four fiducial marks are identifiable on the scanned image, a 2D affine transformation is chosen to remove the linear part of such film deformations. These transformations help correct for geometric distortions and ensure alignment with physical calibration data.

Missing calibration protocol information. When original calibration protocols are unavailable, interior orientation parameters and fiducial mark coordinates are typically missing. However, they can be estimated from auxiliary image data, known scanner resolution and visible fiducial marks. For most images, except the oldest, the principal distance can be retrieved from auxiliary data printed on the image borders. The scanner resolution is usually available, allowing digital images to be scaled accordingly (Fig. 12c).

To unify all scanned images into a common camera coordinate system, fiducial coordinates must be derived. This begins by defining canonical fiducial mark positions based on their locations in the image (e.g., corners or edge midpoints). Their IDs can be assigned arbitrarily (see Fig. 12d, where s is the image width in pixels). Fiducial marks are then measured in each image and transformed to the canonical layout using a rigid 2D transformation (shifts, rotation, but no scaling). Reference fiducial coordinates are calculated by robustly averaging the transformed coordinates, preferably using the median to minimise the impact of film deformations, and then converted from pixels to millimetres using the scanner resolution. These derived reference fiducials are used in SfM or photogrammetric software to define the interior orientation. If residuals after fiducial transformation, e.g., as performed by the software, vary significantly across image groups (e.g., RMS > 0.5 pixels), this may indicate differences in storage or scanning. In such cases, separate fiducial sets and distinct camera models are recommended, even if the images were acquired with the same physical camera.

While early SfM software lacked support for fiducial marks, most modern tools (post-2018) now include this functionality. When fiducials cannot be used, workflows may rely on pre-processing, alignment procedures, or full self-calibration during BBA.

B. Pre-processing techniques

Historical aerial and satellite images require careful pre-processing to improve the accuracy and reliability of stereo reconstruction and feature matching. Although recent tools such as [108] and [109] offer some automation, pre-processing remains largely manual, non-standardised, and inconsistently reported across studies.

Pre-processing involves geometric and radiometric corrections to minimise some challenges associated with historical datasets, standardise inputs for photogrammetric or SfM workflows and enhance feature detection [43], [110].

Among geometric corrections, image masking is widely used, particularly in SfM workflows with aerial imagery, to exclude degraded (e.g., scratches, underexposure) or irrelevant (e.g., borders, annotations, moving objects) portions of the image that could generate false tie points (e.g., [15], [86], [111]). In satellite imagery, masking also helps focus on areas of interest and reduce computational load (e.g.,[112], [113]).

For SfM processing of aerial images, especially when the software does not support fiducial marks, the user must ensure that the image content is stored identically within the files: the edges of the analogue image should be as parallel as possible to the rows and columns of the scanned image (with the auxiliary data always on the same side), and the number of rows and columns in all files must be identical. This way, the image files can be considered as coming from the same 'digital' camera, thereby increasing the robustness of SfM processing [37]. This requires cropping images from the same camera to a consistent extent. Cropping is often followed by transformations based on fiducial marks, including rigid, similarity, or affine transformations, to geometrically align images. Recent updates of SfM software allow more efficient image grouping and transformation using fiducials.

Spy satellite images, especially from KH missions, present additional challenges due to their large format, scanning requirements, and lack of calibration protocols and fiducial marks. Pre-processing often includes stitching the sub-images together. This can be achieved by matching the overlap area between adjacent scans using point-matching techniques, such as SIFT [114], or dense correlation [24]. The rotation and scaling may differ between scans, so correcting for such distortion before the stitching is recommended [43], [114], [115].

Image distortion correction is frequently necessary, as most historical satellite images do not contain true fiducial markers. For the frame camera images (US KH-9 mapping camera, Soviet KFA-1000, KATE-200, or MK-4), black crosses are printed on the images, either on a full réseau grid with a one-centimetre spacing for the KH-9 mapping camera (Fig. 3) or at the centre of the image edges. These crosses can be used to correct distortions using a similarity transformation, as for aerial images. For the KH-9 MC images, the reseau grid enables the correction of film distortion with high accuracy using a Thin-Plate-Spline transformation [24], [114]. For panoramic camera (PC) images (US KH-4/4A/4B, KH-9 PC), the system does not include fiducial markers. However, regularly spaced dots and stripes printed on the edges of the film can be used to correct for film rotation and distortions in the dimension parallel to the camera rotation axis, i.e., along image columns [43], [116]. These markers can also be used to crop the image to the exposed area only.

Radiometric corrections are applied less frequently but can help improve the visibility of fiducial marks and image features [117]. Enhancements include exposure and contrast adjustments (e.g., [118], [119]), vignetting correction [120], and noise reduction from film grain and digitisation artefacts [102], [114]. These adjustments are often made using general image editing tools such as Photoshop, Lightroom, or GIMP [54], [121]. Some studies also employed built-in quality filters in SfM software to exclude suboptimal images [122].

Despite the widespread application of geometric and

radiometric corrections, their quantitative impact on image processing, such as tie point extraction, image orientation, or DEM quality, has not been systematically assessed.

C. Image Processing Workflow type, Software and pipelines

Building on the theoretical principles of classical photogrammetry and SfM, we identified five main workflow categories for processing historical aerial and satellite imagery: Photogrammetric, SfM, Manual, Combined, and Time-SIFT (Fig. 13). The "Combined" methods include datasets processed using both Photogrammetric and SfM solutions (e.g., SocetSet and VisualSFM software, [123]). The "Manual" workflows are custom photogrammetric and SfM pipelines that utilise different software and tools (e.g., Matlab, ORIENT) for image orientation, DEM reconstruction and orthorectification [120], [124]. "Time-SIFT" applies SfM principles to multi-temporal images by jointly estimating interior and exterior orientations across all epochs in a single block before separating the epochs for dense image matching [19]. This method assumes that sufficient inter-epoch tie points remain stable across time.

The reviewed literature reveals a wide range of processing strategies influenced by data availability, software capabilities, often related to their version, and specific project requirements. There are large variations in image orientation and calibration methods, including the use and detection of fiducial marks (Fig. 13), the estimation of unknown camera parameters, and the selection of feature-matching algorithms. Implementation strategies for BBA also vary. Some studies use fixed interior orientation parameters from original calibration reports and others refine them during BBA or self-calibration (e.g., [9], [125], [126], [127]). In other cases [81], a small subset of five aerial images with a good number of well-distributed tie points across the images was pre-calibrated. Then the remaining images were processed with the calibration fixed.

The use of SfM and Photogrammetric processing among the 630 datasets is almost comparable (Fig.13). SfM is the most used method for processing historical aerial images [128], [129], with Agisoft Metashape (formerly Photoscan) the most frequently used software, followed by MicMac and Pix4D (Fig. 13). MicMac is an open-source photogrammetric suite, widely used for both aerial and satellite image processing and supports custom implementations with fiducial mark integration [130].

The use of fiducial marks in aerial SfM workflow has become more common (e.g., [86], [131], [132], [133]), especially with newer tools and software that support their automatic detection (e.g., Agisoft Metashape v1.4.2 onwards). Nonetheless, in many studies, fiducial mark detection or refinement was performed manually. [36] implemented a semi-automatic method using pattern matching to propagate fiducial positions across images. Similarly, [108] applied template-matching techniques for this purpose. Despite their benefit, fiducial marks were not used in approximately 25% of the datasets, often due to missing calibration data or software limitations.

Photogrammetric methods are also widely used, but they require known or approximated interior and exterior orientation parameters (Fig. 12a). In several aerial studies where the camera positions were unknown, alternative solutions followed the workflow in Fig. 12c or employed an automatic resection process using the GCP-based geometric model (e.g., [134]). In other cases, SfM software was used to derive approximate values of external orientation (e.g., [135]). For spy satellite images, the only information available is the nominal focal length stated in the declassified documentation and a maximum distortion value. To circumvent this missing information, the camera focal length and distortion are usually estimated during BBA using automatic tie points and possibly manual GCPs for each scene processed (e.g., [114], [136]). [24] estimated these parameters for all KH-9 MC missions using a combined BBA on approximately 600 images covering different parts of the globe and automatically extracting GCPs. This ensures that the camera models are consistent within a single mission, assuming that no significant changes occurred to the system during the satellite lifetime (up to a maximum of 6 months). Additionally, the results showed that the estimated focal length differed by up to 2.7 mm from the nominal value (304.8 mm), stressing the need to refine the focal length during BBA.

ERDAS Imagine Photogrammetry and its predecessors are the most popular photogrammetric software (Fig. 13) for manual or semi-automated orientation of aerial and satellite images, as it offers a high level of flexibility in model selection during bundle adjustment. Specifically for Corona stereo-imagery, which is affected by film distortions and has limited camera information, the non-metric camera model implemented in ERDAS Leica Photogrammetric Suite was used to geometrically correct and solve the relative orientation of the stereo-imagery (e.g., [69], [98], [137], [138]). The required information was the focal length, pixel size of the scanned images, and flight altitude of the camera platform, while the exterior orientation was solved using GCPs. Recently, GCPs have also been used in methods for correcting and orthorectifying Corona images [44].

The orientation of Corona and Hexagon imagery has evolved from these manual approaches toward fully automated pipelines [24], [43], [114]. An overview of the earlier work on the camera orientation of Corona images can be found in [43]. Recently, two automated processing pipelines have been developed: the "Corona Stereo Pipeline" (CoSP) by [43] and "automatic orientation and orthorectification" (2OC) by [139]. CoSP implements a rigorous Corona camera model and automates processing over the entire Corona image swath and in multi-image configurations. The 2OC for Corona KH-4B Panoramic Imagery is based on a 14-parameter panoramic mathematical model and a time-iterative orthorectification technique to correct the panoramic geometric distortion and fit the focal length distortions of Corona panoramic images.

In contrast to Corona imagery, Hexagon KH-9 mapping camera images are easier to process due to the frame camera geometry and the availability of a reseau grid to estimate film distortions [140]. Recently, open-source pipelines have been developed for the Hexagon spy satellite, such as HEXIMAP - Hexagon Imagery Automated Pipeline [114] and Ames Stereo Pipeline [141], employed by [142] and [24]. The latter developed an automated workflow using Ames Stereo Pipeline

to process scanned images from the KH-9 Hexagon mapping camera, deriving the focal length and lens parameters for each KH-9 mission and generating DEMs.

D. Georeferencing strategies

Almost all datasets included GCPs in their processing. Nearly 90% of datasets used between 3 and 100 GCPs, with some country and regional scale studies using thousands of GCPs manually or automatically detected (e.g., [54], [97], [120], [124], [125], [143]).

GCPs are necessary to place, rotate and scale the block of images in 3D space, a process known as absolute orientation (Fig. 11). For this basic purpose of absolute orientation, only seven GCP coordinates are needed, and thus, having one GCP in each corner of a rectangular block of images, i.e. four sets of 3 coordinates, is already more than needed, at least in principle. Nevertheless, having (much) more than this minimum amount of ground control is indeed beneficial and recommended since more GCPs increase the reliability, i.e. the ability to detect gross errors in the data (especially in the set of GCPs). Additionally, when GCPs are included in the BBA, more GCPs also increase the accuracy of the photogrammetric reconstruction by constraining the reconstructed area around GCPs to be close to these GCPs, thereby preventing what is known as the “dome effect” (e.g., [144], [145], [146]). This effect shows up as bending error in (large) areas without GCPs and results from the accumulation of minimal residual systematic errors in the entire data set. A sparser arrangement of GCPs along the border can be compensated to some degree by extending the original block of images by one strip on each long side of the block and two images at the beginning and end of each strip [147].

Generally, GCPs should fulfil the following conditions: 1) be well defined so that they can be well identified in the historical images, 2) their 3D coordinates should be as accurate as possible, and 3) be well distributed over the block area, to constrain the geometry of the image block.

Well-defined and highly accurate GCPs would necessitate in-situ measurements, such as using GNSS (i.e., a point-based source). However, due to storage deformation and radiometric quality, the achievable accuracy will be at best the decimeter level for archival aerial images and up to the decameter level for historical satellite images. Therefore, to avoid in-situ measurements, recent orthophotos with a pixel size of 1-2 dm and a DEM should be sufficient to derive GCPs' horizontal and vertical coordinates, in a temporally stable area (i.e., an area-based source). The considered papers in this study primarily follow this approach. However, detailed information about the type of GCPs and their related accuracy is scarce (only reported for approximately 40% of the datasets processed), preventing a quantitative comparison. Nonetheless, for point-based ground control, decimeter accuracy up to 1 m is reported, while for area-based ground control, accuracies are in the metre range, up to 10 m (depending on the source of the elevation information).

Most studies used manually identified GCPs, although a few studies have explored automated GCP identification. These implemented approaches can be grouped into two categories. One approach is based on automatically identifying GCPs in auxiliary orthophotos acquired at a different time [97], sometimes leveraging machine learning techniques (e.g., [31], [43], [116], [148]). Another approach involves generating an initial DEM using coarse flight information and then co-registering the DEM with auxiliary elevation data using affine transformations. These transformations can then be used to refine camera external parameters (e.g., [24], [36], [108]).

E. Post-processing techniques

To improve the quality (accuracy and completeness) of photogrammetrically derived products, post-processing procedures such as co-registration, point cloud refinement, noise filtering, and gap filling are often applied. Some of these steps are applied to the point cloud before DEM generation or directly to the DEM. This section focuses on co-registration and noise filtering.

Co-registration. Photogrammetric products often exhibit residual systematic errors, regardless of whether SfM or classical photogrammetry is used [149] and despite the high number of GCPs and low RMSE values achieved after BBA optimisation. Random errors in exterior orientation can propagate into linear biases in DEMs [150], which can be mitigated by accurate GCPs [127] but typically require correction using reference data [151]. In the reviewed studies, airborne LiDAR and high-accuracy DEMs are preferred as references (e.g., [72], [126], [152]), although often the availability of data for the area of interest determines the choice of reference data. Global datasets like SRTM DEM are often used for spy satellites in data-scarce regions such as High Mountain Asia (e.g., [153], [154]).

The primary co-registration approaches involve identifying stable terrain to estimate transformation parameters (translation, rotation, scaling) between DEMs. Common algorithms include least-squares point matching (e.g., [117], [149]) and iterative closest point (ICP; e.g., [155], [156]), often implementing Helmert transformations [157]. The algorithm in [158], which is widely used in glaciology, is implemented in several repositories (e.g., *demcoreg*, [159]; xDEM, [160]) and corrects for translation using slope-aspect regression but cannot fully address rotation [161], which some studies mitigate using trend surface fitting (e.g., [110], [154]). A least-Z difference algorithm is newly implemented in xDEM.

Most studies have computed the elevation difference between the reference and the derived historical DEM to quantify this bias or used cloud-to-cloud differences (e.g., the M3C2 algorithm, [162]) before and after co-registration. Improvements after post-co-registration range from decimeters to 2 m for aerial data and up to 6 m for spy satellite imagery ([149], [154]). However, the magnitude of bias correction depends on factors such as the acquisition year of the images and the region [149].

Noise filtering. Noise and blunders are common in 3D photogrammetric data, especially from scanned historical images, which degrade DEM quality and increase uncertainty.

Various methods have been employed, although only a few studies have detailed their removal. Filtering is applied to the original point cloud and/or the DEM, and automatic tie points were filtered before BBA optimisation (e.g., [122]). Manual dense point cloud filtering is a common approach (e.g., [83], [163]), whereas others rely on built-in filters in software such as Agisoft or ERDAS (e.g., [164]). CloudCompare's statistical outlier removal tool ([165]) is also frequently used (e.g., [127], [166]). Additionally, height thresholds relative to reference data or DTMs also help eliminate vegetation and spurious points. [167] employed Delaunay triangulation for noise reduction. [122] demonstrated that removing low-confidence points (values < 4) and using less aggressive depth map filters improved accuracy but reduced point cloud density. Subsampling and duplicate point removal were also applied before rasterization.

In all cases, noise filtering introduces gaps, often filled via raster interpolation. The TIN method facilitates the easy identification of interpolated areas, whereas in glaciology, hypsometric interpolation of elevation difference maps is a common practice [168].

VI. Accuracy assessment of historical image products

The minimum setup for a photogrammetric reconstruction is two images. If the viewing directions of these two images are parallel and orthogonal to the line connecting both projection centres, then this setup is termed the photogrammetric normal case. Following [106], using the photogrammetric normal case planimetric coordinates (x and y) of object points may then be reconstructed with an accuracy of roughly

$$\sigma_x = \sigma_y = \sigma_{ref} = GSD \times \sigma_{image} \ . \quad (1)$$

Critical for this estimation is σ_{image}, the image measurement accuracy, which specifies the accuracy for identifying and measuring points in the images. Usually, σ_{image} is in the range between 0.1 pix and 1 pix. If the image quality is poor or the film deformations cannot be compensated well, then σ_{image} may be much worse. A good estimate for σ_{image} can be obtained after BBA using the root of the reference variance σ_{ref} or the mean reprojection error. A practical example using the following values should clarify these theoretical numbers: an image scale of 1:20.000, a scanning resolution of 14 µm (yielding GSD = 28 cm), and an assumed σ_{image} of 0.5 pix. From equation (1), we then get σ_{ref} = 0.5*28 cm = 14 cm.

The accuracy in height for this photogrammetric normal case is generally worse than in planimetry and can be estimated as:

$$\sigma_z = H/B \ \sigma_{ref} \quad (2)$$

Here, H is the flying height above the terrain, and base B is the distance between the two projection centres.

Understanding the accuracy and resolution of historical image-derived products is relevant for interpreting detected changes. However, the reviewed literature reveals wide variability in how data quality is reported, making cross-study comparisons difficult. Accuracy assessments vary due to differences in reference data, reporting practices, and statistical metrics. To standardise analysis, reference datasets were categorised as area- or point-based and sourced from terrestrial (e.g., RTK-GNSS, TLS), airborne, satellite (e.g., Pléiades, SRTM), altimetry, or topographic maps.

Root mean square error (RMSE) and standard deviation were the most commonly reported metrics for DEM accuracy, and we relied on these two metrics for cross-study comparisons (Fig. 14). Among 630 datasets across 198 studies, fewer than half included both vertical accuracy and reference data quality, limiting the ability to assess trends, especially for satellite-based products. On average, aerial image-derived DEMs showed roughly six times better accuracy than those from satellite data (2.98 m vs 18.9 m, with corresponding standard deviations of 5.9 and 14.7 m), reflecting differences in resolution and image quality.

One key research question of this study was to assess how factors such as pre-processing steps, processing approach (e.g., SfM vs. photogrammetry), fiducial mark usage, GCP quantity and accuracy, GSD and scanner settings influence the accuracy of historical products. Although inconsistent reporting limited direct comparisons, some insights can be drawn.

A. SfM vs Classical Photogrammetry

Comparisons between SfM and classical photogrammetry (e.g., [149], [169]) found no clear accuracy advantage for either method, despite suboptimal acquisition conditions. Similarly, the use of fiducial marks in the reviewed studies does not reveal a clear increase in vertical accuracy (Fig. 14), which is unexpected, as using fiducials should lead to a more accurate estimation of the interior camera geometry. However, other factors like image quality and reference data uncertainty may have hidden any potential positive relationship between using fiducial marks and accuracy.

B. Influence of Ground Sampling Distance (GSD)

The GSD and accuracy of the 3D reconstruction are interlinked, equation (1). This interlinkage can be demonstrated by considering the ratio between reported accuracy and GSD. Fig. 15 shows that the larger the GSD, the larger the reported residuals. The higher resolution of the datasets with lower GSD enables surface reconstruction with higher detail and, consequently, lower interpolation errors. However, it is also evident that exceptions occur due to other influencing factors, such as image quality, scanning resolution, and processing methods.

C. GCPs and self-calibrating models

Reference [170] recommended using 6–9 GCPs per stereo pair for self-calibrating bundle adjustment, although 12 to 16 GCPs may be necessary for very old, small-scale images. Accuracy tends to decline outside the GCP-covered area [134]. The choice of optimal self-calibration method depends on the image scale and characteristics of each historical flight. In the study by [170], the lens distortion model, closely following Brown's model, performed best. However, it is recommended to test other models, as each flight may have different systematic errors. Nevertheless, the number and quality of GCPs used in the bundle adjustment have a greater impact on

the results than the self-calibration model [171]. Studies confirmed that GCP accuracy, can directly impact DEM accuracy and should not be lower than the image GSD [169].

D. Impact of scanning settings on DEM Accuracy

Image digitisation quality critically affects the performance of photogrammetric reconstruction and DEM accuracy. Reference [172] found that higher scanning resolutions improved point cloud density and reduced errors. The mean dense point cloud density increased from 0.3 to 11 points/m² using a 400 vs 2400 dpi scanner, resulting in 2 m and 0.35 m DEM resolutions, respectively. There was negligible improvement between 1600 and 2400 dpi, which only increased data size without proportional accuracy improvements. Optimal results were achieved with 1600 dpi for 8-bit and 800 dpi for 16-bit images [164]. Excessively high resolutions increased data size without corresponding improvements in accuracy. Similarly, studies (e.g., [11], [32], [171]) have shown that lower-cost or non-photogrammetric scanners can reduce accuracy by up to threefold. Scanner-induced distortions, such as subpixel shifts or radiometric inconsistencies, can also compromise DEM accuracy. Spy satellite studies have reported scan tile misalignments and pixel-level shifts, even with photogrammetric-grade scanners [24], [25].

VII. Emerging trends and technological advances

Processing historical images for accurate orthoimages and DEMs remains an open research task. Recent developments focus on two fronts: improving feature matching through open-source deep learning algorithms and automating georeferencing solutions.

The successful image orientation largely depends on robust feature matching [21], [173]. Traditional methods like SIFT often fail under temporal or camera variations [174]. Time-invariant line (TIL) features [9] or multimodal matching [175] have been recently proposed. However, learning-based algorithms, including SuperGlue [176], DISK [177], and hybrid pipelines [178] have proven more robust for wide-baseline and low-texture image matching. These were evaluated by [179] and [174] using historical datasets and implemented by [21], who proposed a pipeline that requires no prior metadata, such as DSMs or focal lengths.

Automated georeferencing and GCPs extraction are another major advance (see Section VD). Reference [97] integrated an external orthophoto and DEM for automatic GCPs extraction. Another established automated method is tie-point matching between recent georeferenced images and historical non-georeferenced images to automatically retrieve GCPs. Reference [180] used the LightGlue algorithm to derive common tie-points from Sentinel-2 imagery and aerial images, while [43] used SuperGlue to match Corona KH-4 images to modern satellite data in their CoSP pipeline.

The most automated solution to georeference the image block and simultaneously estimate the camera orientation is developed in HSfM [108], which combines the Time-SIFT approach with a multi-stage co-registration process of the estimated historical image DEMs to a reference DEM to optimise camera orientation without GCPs. They claim that the processing of multiple datasets improves the final quality. A similar solution has already been developed by [24] for KH-9 DEM.

Multi-epoch approaches can struggle where stable terrain is lacking [181]. To overcome this issue, coarse-to-fine matching strategies have recently been developed, combining 2D patch-based [182] and 3D DSM-based matching [148], also leveraging SuperGlue within the MicMac framework.

Beyond geometry improvements, historical images enhancements in radiometry and semantics are expanding. CNNs have been applied to optimise contrast [183], correct radiometry without metadata [184], and colourise grayscale imagery [174]. Semantic enrichment via deep learning (e.g., U-net) enables more detailed content extraction [180]. Other studies address specific challenges in spy satellite imagery, such as tree visibility [185] or urban mapping [186]. Yet, issues like low radiometric depth, shadows, and saturation still limit output quality.

VIII. Recommendations for processing and accuracy assessment

Processing historical aerial imagery remains challenging due to the heterogeneity of datasets, dataset-specific issues, and often images do not meet standard photogrammetric requirements [22], [50]. Despite growing interest, there is still no consensus on standardised processing or accuracy assessment methods [20], [21].

A critical next step is to evaluate existing workflows or develop new pipelines tailored to different dataset types. Sensitivity analyses are necessary to understand how pre-processing decisions, metadata availability, feature-matching algorithms, and georeferencing approaches impact the final accuracy. To facilitate this, the European Spatial Data Research (EuroSDR) launched the TIME (hisTorical aerIal iMagEs) benchmark initiative [187], offering shared datasets and fostering collaboration through workshops that connect researchers, archives, and industry [174].

Photogrammetric workflows, despite being highly evolved, can still introduce systematic and random errors at various stages, making it challenging to compare the quality of DEMs and orthoimages across studies. Many assessments rely on simplified metrics, such as mean reprojection error or pseudo-ground truth generated from input images [188], which often poorly correlate with external topographic control data [179].

A common accuracy assessment method involves comparing historical DEMs with reference elevation datasets over assumed stable areas (or points). However, such assessments often combine systematic and random errors, underestimating uncertainties. Reference [189] demonstrated that conventional metrics, like standard deviation, fail to capture spatially correlated or terrain-dependent errors. To address this, they developed a method implemented in the open-source Python package xDEM [160] that characterises DEM precision through measures of heteroscedasticity and spatially correlated error.

To ensure comparability and transparency in future studies, a minimum set of reporting requirements should be adopted. This

includes detailed documentation of:

- Image information such as number of images, acquisition dates, ground sampling distance (and/or image scale), metadata, and image archive.
- GCPs number, collection method, spatial distribution, horizontal/vertical accuracy, and related metrics.
- Reference data for accuracy assessment or post-processing, including its vertical and horizontal accuracy, even when publicly available DEMs are used as reference. Information on the stable areas or number, and related accuracy of check points and their spatial distribution.
- DEM accuracy assessment methods and post-processing steps.
- Accuracy metrics, reporting mean and median elevation differences to identify systematic errors in generated DEMs. These metrics should be calculated after co-registration procedures.
- Precision metrics should consider robust statistics, such as the Normalised Median Absolute Deviation (NMAD) and the confidence interval (typically 95%). Ideally, the frequency distribution of the error should also be reported, including spatially correlated error [189].
- Fully documented workflow ideally supported by accessible and reproducible code.

IX. Unlocking image archives and data availability

Our review of 198 studies reveals that only a fraction of the images available in archives worldwide have been (re-)processed. This underscores the vast untapped potential of historical imagery for environmental research.

The fragmentation and inaccessibility of archives, as well as the digitisation and costs of scanned images, are the two key challenges to unlocking the full potential of historical photographs. As early as 1997, [13] warned of the ongoing deterioration of historical (aerial) photography and the need for immediate action in preserving this material. Since then, access to historical photography has undergone significant changes due to the emergence of digital collections and online queries [190]. Yet, a global inventory of these archives remains absent, complicated by the fragmentation of multiple archives even within a single country that holds the same or different datasets varying in quality and coverage. A EuroSDR analysis [8] revealed that most European archives have processed less than half of their analogue image collections; for example, NCAP has only digitised 2% of their images as of 2019.

To make these photographs more accessible, geospatial cataloguing and tools, reporting image footprints, acquisition dates, overlaps, and flight characteristics, as well as metadata, are crucial. Web platforms that offer such tools, like Swisstopo [191], NARA [192] or USGS Earth Explorer, improve accessibility by enabling geo-referenced search and visualisation.

However, accessibility challenges remain. Many archives charge fees for scanned images or basic consultation, limiting their use for large areas. Scanning is particularly labour-intensive, requiring skilled operators and high-quality (ideally photogrammetric) scanners. Most European archives have access to such scanners, and costs can reach €50 per photo. Given these financial and logistical constraints, national-level support is essential to ensure the preservation, digitisation, and open dissemination of this valuable historical resource.

Conclusion

We reviewed studies that deal with the digital photogrammetric processing of historical stereo-images taken from analogue cameras mounted on airborne and spy satellites. Most aerial images date from World War I to the early 2000s, while spy satellite images date from approximately 1960 to late 1990. These millions of aerial and satellite photographs are undoubtedly the largest, almost unexploited remote sensing resource available to geoscientists, with huge potential to document and quantify surface changes over the past century. With their high resolution, repeat surveying, worldwide coverage, and stereoscopic acquisition, these historical images are ideal for long-term environmental monitoring and change detection by generating three-dimensional (DEM) and two-dimensional (orthophoto) data. Combined with modern remote sensing data, these long-term series datasets enable the quantification of earth surface processes, human activities, and landscape evolution, providing valuable calibration data for modelling surface processes in future climate scenarios.

Despite growing awareness of their value, as demonstrated by the increasing number of studies within the geoscience community, several obstacles remain to their fuller exploitation. These challenges can be summarised by 1) limited online accessibility and queries to the images, 2) scanning procedure and availability of metadata, 3) their costs, 4) large variations in radiometric and geometric image quality, and 5) the open access and reproducibility of solutions to process historical images accurately.

This review enhances accessibility to historical imagery by providing information about the challenges associated with these datasets, and processing solutions for creating orthophotos and DEMs from stereo historical images adopted over the past 20 years. The focus is on recent automated pipelines for processing aerial and spy satellite images. SfM technology has opened new possibilities, and studies have found that DEMs generated using SfM can achieve accuracy comparable to that derived from traditional photogrammetry. However, the reported accuracy must be more consistent for meaningful comparisons to be made. Advances in artificial intelligence solutions are being developed to solve some of the challenges of processing historical images, such as feature matching and GCP detection.

Our study suggests areas for future research, from unlocking image archives by improving online access and offering low or free accessibility to developing efficient, accessible, and reproducible workflows to convert historical photographs into high-quality digital spatial data on a large scale. Increasing accessibility and usability is crucial for making these unique datasets available to a broad range of users, thereby enabling

more widespread application in geosciences and beyond.

ACKNOWLEDGMENT

LP, RM, ME, CR, AD, LG, TD, and AE formulated the research questions and designed the project. RM created the database linked to the Zotero repository. All co-authors reviewed the published papers and contributed to filling the database. LP, RM, and ME analysed the database; LP, RM, ME, CR, and AE interpreted the results. LP, RM, ME, CR, and AD prepared the published figures and tables. LP drafted the original manuscript, and RM, ME, CR, AD, and AE contributed to specific sections. LP, RM, AD and CR wrote the supplementary text. All co-authors provided feedback on the manuscript.

REFERENCES

[1] K. C. Ruffner, 'Corona: America's First Satellite Program', *1995*, vol. Morgan James Publishing.

[2] J. H. Chandler and D. Brunsden, 'Steady state behaviour of the Black Ven mudslide: The application of archival analytical photogrammetry to studies of landform change', *Earth Surf. Process. Landf.*, vol. 20, no. 3, pp. 255–275, 1995, doi: 10.1002/esp.3290200307.

[3] E. Schiefer and R. Gilbert, 'Reconstructing morphometric change in a proglacial landscape using historical aerial photography and automated DEM generation', *Geomorphology*, vol. 88, no. 1, pp. 167–178, Jul. 2007, doi: 10.1016/j.geomorph.2006.11.003.

[4] A. Schaffland and G. Heidemann, 'Heritage and Repeat Photography: Techniques, Management, Applications, and Publications', *Heritage*, vol. 5, no. 4, Art. no. 4, Dec. 2022, doi: 10.3390/heritage5040220.

[5] J. Casana, 'Global-Scale Archaeological Prospection using CORONA Satellite Imagery: Automated, Crowd-Sourced, and Expert-led Approaches', *J. Field Archaeol.*, vol. 45, no. sup1, pp. S89–S100, Feb. 2020, doi: 10.1080/00934690.2020.1713285.

[6] E. Hammer, M. FitzPatrick, and J. Ur, 'Succeeding CORONA: declassified HEXAGON intelligence imagery for archaeological and historical research', *Antiquity*, vol. 96, no. 387, pp. 679–695, Jun. 2022, doi: 10.15184/aqy.2022.22.

[7] J. L. Morgan, S. E. Gergel, and N. C. Coops, 'Aerial Photography: A Rapidly Evolving Tool for Ecological Management', *BioScience*, vol. 60, no. 1, pp. 47–59, Jan. 2010, doi: 10.1525/bio.2010.60.1.9.

[8] S. Giordano and C. Mallet, 'Archiving and geoprocessing of historical aerial images: current status in Europe', *EuroSDR Off. Publ. No*, vol. 70, 2019.

[9] S. Nagarajan and T. Schenk, 'Feature-based registration of historical aerial images by Area Minimization', *ISPRS J. Photogramm. Remote Sens.*, vol. 116, pp. 15–23, Jun. 2016, doi: 10.1016/j.isprsjprs.2016.02.012.

[10] E. S. Mannerfelt *et al.*, 'Halving of Swiss glacier volume since 1931 observed from terrestrial image photogrammetry', *The Cryosphere*, vol. 16, no. 8, pp. 3249–3268, Aug. 2022, doi: 10.5194/tc-16-3249-2022.

[11] A. Kostrzewa, E. M. Farella, L. Morelli, W. Ostrowski, F. Remondino, and K. Bakuła, 'Digitizing Historical Aerial Images: Evaluation of the Effects of Scanning Quality on Aerial Triangulation and Dense Image Matching', *Appl. Sci.*, vol. 14, no. 9, Art. no. 9, Jan. 2024, doi: 10.3390/app14093635.

[12] C. Munteanu *et al.*, 'The potential of historical spy-satellite imagery to support research in ecology and conservation', *BioScience*, vol. 74, no. 3, pp. 159–168, Mar. 2024, doi: 10.1093/biosci/biae002.

[13] D. E. Luman, C. Stohr, and L. Hunt, 'Digital reproduction of historical aerial photographic prints for preserving a deteriorating archive', *Photogramm. Eng. Remote Sens.*, vol. 63, no. 10, pp. 1171–1179, 1997.

[14] P. Redweik, D. Roque, A. Marques, R. Matildes, and F. Marques, 'Recovering Portugal aerial images repository', in *The International Archives of the Photogrammetry, Remote Sensing and Spatial Information Sciences*, Hannover, Germany, 2009, p. 6.

[15] A. Riquelme, M. Del Soldato, R. Tomás, M. Cano, L. Jordá Bordehore, and S. Moretti, 'Digital landform reconstruction using old and recent open access digital aerial photos', *Geomorphology*, vol. 329, pp. 206–223, Mar. 2019, doi: 10.1016/j.geomorph.2019.01.003.

[16] S. Ullman, 'The interpretation of structure from motion', *Proc. R. Soc. Lond. B Biol. Sci.*, vol. 203, no. 1153, pp. 405–426, Jan. 1979, doi: 10.1098/rspb.1979.0006.

[17] A. Eltner and G. Sofia, 'Structure from motion photogrammetric technique', in *Developments in Earth Surface Processes*, vol. 23, Elsevier, 2020, pp. 1–24. doi: 10.1016/B978-0-444-64177-9.00001-1.

[18] N. Micheletti, S. N. Lane, and J. H. Chandler, 'Application of archival aerial photogrammetry to quantify climate forcing of alpine landscapes', *Photogramm. Rec.*, vol. 30, no. 150, pp. 143–165, Jun. 2015, doi: 10.1111/phor.12099.

[19] D. Feurer and F. Vinatier, 'Joining multi-epoch archival aerial images in a single SfM block allows 3-D change detection with almost exclusively image information', *ISPRS J. Photogramm. Remote Sens.*, vol. 146, pp. 495–506, Dec. 2018, doi: 10.1016/j.isprsjprs.2018.10.016.

[20] A. Le Bris, S. Giordano, and C. Mallet, 'CNN Semantic Segmentation to Retrieve Past Land Cover out of Historical Orthoimages and DSM: First Experiments', *ISPRS Ann. Photogramm. Remote Sens. Spat. Inf. Sci.*, vol. V-2–2020, pp. 1013–1019, Aug. 2020, doi: 10.5194/isprs-annals-V-2-2020-1013-2020.

[21] F. Maiwald, D. Feurer, and A. Eltner, 'Solving photogrammetric cold cases using AI-based image matching: New potential for monitoring the past with historical aerial images', *ISPRS J. Photogramm. Remote Sens.*, vol. 206, pp. 184–200, Dec. 2023, doi: 10.1016/j.isprsjprs.2023.11.008.

[22] D. C. Cowley and B. B. Stichelbaut, 'Historic Aerial Photographic Archives for European Archaeology', *Eur. J. Archaeol.*, vol. 15, no. 2, pp. 217–236, 2012, doi: 10.1179/1461957112Y.0000000010.

[23] M. Fradley, 'British inter-war aerial photogrammetric mapping in the MENA region: archives, access and

research potential', *Levant*, vol. 53, no. 3, pp. 336–346, Sep. 2021, doi: 10.1080/00758914.2021.1992879.

[24] A. Dehecq *et al.*, 'Automated Processing of Declassified KH-9 Hexagon Satellite Images for Global Elevation Change Analysis Since the 1970s', *Front. Earth Sci.*, vol. 8, no. November, p. 516, 2020, doi: 10.3389/feart.2020.566802.

[25] W. Gheyle, J. Bourgeois, R. Goossens, and K. Jacobsen, 'Scan problems in digital CORONA satellite images from USGS archives', *Photogramm. Eng. Remote Sens.*, vol. 77, no. 12, pp. 1257–1264, 2011, doi: 10.14358/PERS.77.12.1257.

[26] J. H. Chandler and M. a. R. Cooper, 'The Extraction of Positional Data from Historical Photographs and Their Application to Geomorphology', *Photogramm. Rec.*, vol. 13, no. 73, pp. 69–78, 1989, doi: 10.1111/j.1477-9730.1989.tb00647.x.

[27] J. H. Chandler and J. S. Clark, 'The Archival Photogrammetric Technique: Further Application and Development', *Photogramm. Rec.*, vol. 14, no. 80, pp. 241–247, 1992, doi: https://doi.org/10.1111/j.1477-9730.1992.tb00249.x.

[28] R. Ferrer Velasco *et al.*, 'Towards accurate mapping of forest in tropical landscapes: A comparison of datasets on how forest transition matters', *Remote Sens. Environ.*, vol. 274, p. 112997, Jun. 2022, doi: 10.1016/j.rse.2022.112997.

[29] J. L. Carrivick and M. W. Smith, 'Fluvial and aquatic applications of Structure from Motion photogrammetry and unmanned aerial vehicle/drone technology', *WIREs Water*, vol. 6, no. 1, p. e1328, 2019, doi: 10.1002/wat2.1328.

[30] E. Rupnik, F. Nex, I. Toschi, and F. Remondino, 'Aerial multi-camera systems: Accuracy and block triangulation issues', *ISPRS J. Photogramm. Remote Sens.*, vol. 101, pp. 233–246, Mar. 2015, doi: 10.1016/j.isprsjprs.2014.12.020.

[31] F. Dahle, R. Lindenbergh, and B. Wouters, 'Polar perspectives: a deep dive into geo-referencing historical Antarctic photos', *Int. J. Digit. Earth*, vol. 17, no. 1, p. 2406384, Dec. 2024, doi: 10.1080/17538947.2024.2406384.

[32] C. Sevara, 'Capturing the Past for the Future: an Evaluation of the Effect of Geometric Scan Deformities on the Performance of Aerial Archival Media in Image-based Modelling Environments: Capturing the Past for the Future', *Archaeol. Prospect.*, vol. 23, no. 4, pp. 325–334, Oct. 2016, doi: 10.1002/arp.1539.

[33] M. Fischer, 'A Short Guide to Film Base Photographic Materials: Identification, Care, and Duplication', Northeast Document Conservation Center. Accessed: Dec. 29, 2024. [Online]. Available: https://www.nedcc.org/free-resources/preservation-leaflets/5.-photographs/5.1-a-short-guide-to-film-base-photographic-materials-identification,-care,-and-duplication

[34] S. Różycki, A. K. Karwel, and Z. Kurczyński, 'German Extermination Camps on WWII Reconnaissance Photographs. Orthorectification Process for Archival Aerial Images of Cultural Heritage Sites', *Remote Sens.*, vol. 15, no. 10, p. 2587, May 2023, doi: 10.3390/rs15102587.

[35] M. Broadbent, 'Reconstructing the Past in 3D Using Historical Aerial Imgery', Master of Science, University of Redlands, Redlands, CA, 2017. doi: 10.26716/redlands/master/2017.2.

[36] S. Giordano, A. Le Bris, and C. Mallet, 'Toward Automatic Georeferencing of Archival Aerial Photogrammetric Surveys', *ISPRS Ann. Photogramm. Remote Sens. Spat. Inf. Sci.*, vol. IV–2, pp. 105–112, May 2018, doi: 10.5194/isprs-annals-IV-2-105-2018.

[37] R. Ma, 'Historical Photograph Orthorectification Using SfM for Land Cover Change Analysis', *J. Indian Soc. Remote Sens.*, p. 11, 2020.

[38] R. Goossens, A. De Wulf, J. Bourgeois, W. Gheyle, and T. Willems, 'Satellite imagery and archaeology: the example of CORONA in the Altai Mountains', *J. Archaeol. Sci.*, vol. 33, no. 6, pp. 745–755, Jun. 2006, doi: 10.1016/j.jas.2005.10.010.

[39] A. Altmaier and C. Kany, 'Digital surface model generation from CORONA satellite images', *ISPRS J. Photogramm. Remote*, vol. 56, no. 4, pp. 221–235, 2002, doi: 10.1016/S0924-2716(02)00046-1.

[40] G. Bitelli and V. A. Girelli, 'Metrical use of declassified satellite imagery for an area of archaeological interest in Turkey', *J. Cult. Herit.*, vol. 10, pp. e35–e40, Dec. 2009, doi: 10.1016/j.culher.2009.08.004.

[41] N. Galiatsatos, D. N. M. Donoghue, and G. Philip, 'An evaluation of the stereoscopic capabilities of CORONA declassified spy satellite image data', in *25th EARSeL symposium, workshop on 3D remote sensing*, Porto, Portugal, 2005, p. 8.

[42] H. G. Sohn, G. I. H. Kim, and J. H. Yom, 'Mathematical modelling of historical reconnaissance CORONA KH-4B imagery', *Photogramm. Rec.*, vol. 19, no. 105, pp. 51–66, 2004, doi: 10.1046/j.0031-868X.2003.00257.x.

[43] S. Ghuffar, T. Bolch, E. Rupnik, and A. Bhattacharya, 'A Pipeline for Automated Processing of Declassified Corona KH-4 (1962–1972) Stereo Imagery', *IEEE Trans. Geosci. Remote Sens.*, vol. 60, pp. 1–14, 2022, doi: 10.1109/TGRS.2022.3200151.

[44] G. Molnár, 'Orthocorrection of Corona KH-1 Satellite Panoramic Images', in *2023 IEEE 21st World Symposium on Applied Machine Intelligence and Informatics (SAMI)*, IEEE, 2023, pp. 000231–000236. doi: 10.1109/SAMI58000.2023.10044516.

[45] D. C. Cowley, R. A. Standring, and M. J. Abicht, 'Landscapes through the lens: An introduction', in *Landscapes Through the Lens: Aerial Photographs and Historic Environment*, D. C. Cowley, R. A. Standring, and M. J. Abicht, Eds., United Kingdom: Oxbow Books, 2010, pp. 1–6.

[46] D. Cowley and L. Ferguson, 'Historic aerial photographs for archaeology and heritage management', in *Space Time and Place: Proceedings of the III International Conference on Remote Sensing in Archaeology*, Tiruchirappalli, Tamil Nadu, India: BAR Publishing, 2009, pp. 17–21.

[47] NARA, 'Aerial Photography', National Archives. Accessed: Oct. 16, 2024. [Online]. Available:

https://www.archives.gov/research/cartographic/aerial-photography

[48] NCAP, 'History of the Collection', National Collection of Aerial Photography. Accessed: Oct. 16, 2024. [Online]. Available: https://ncap.org.uk/about-ncap/history-of-the-collection

[49] NARA, 'Aerial Photographs, 1935 - 1970', US Flown Foreign Aerial Photography in Record Group 373: Records of the Defense Intelligence Agency. Accessed: Mar. 24, 2025. [Online]. Available: https://www.archives.gov/research/cartographic/aerial-photography/rg-373-dia-foreign-aerial-photography

[50] C. Gomez, Y. Hayakawa, and H. Obanawa, 'A study of Japanese landscapes using structure from motion derived DSMs and DEMs based on historical aerial photographs: New opportunities for vegetation monitoring and diachronic geomorphology', *Geomorphology*, vol. 242, pp. 11–20, Aug. 2015, doi: 10.1016/j.geomorph.2015.02.021.

[51] R. C. Carvalho, B. Allan, D. M. Kennedy, C. Leach, S. O'Brien, and D. Ierodiaconou, 'Quantifying decadal volumetric changes along sandy beaches using improved historical aerial photographic models and contemporary data', *Earth Surf. Process. Landf.*, vol. 46, no. 10, pp. 1882–1897, Apr. 2021, doi: https://doi.org/10.1002/esp.5130.

[52] N. Kulha, L. Pasanen, and T. Aakala, 'How to Calibrate Historical Aerial Photographs: A Change Analysis of Naturally Dynamic Boreal Forest Landscapes', *Forests*, vol. 9, no. 10, p. 631, Oct. 2018, doi: 10.3390/f9100631.

[53] K. D. Fieber, J. P. Mills, P. E. Miller, L. Clarke, L. Ireland, and A. J. Fox, 'Rigorous 3D change determination in Antarctic Peninsula glaciers from stereo WorldView-2 and archival aerial imagery', *Remote Sens. Environ.*, vol. 205, pp. 18–31, Feb. 2018, doi: 10.1016/j.rse.2017.10.042.

[54] E. C. Geyman, W. J. J. van Pelt, A. C. Maloof, H. F. Aas, and J. Kohler, 'Historical glacier change on Svalbard predicts doubling of mass loss by 2100', *Nature*, vol. 601, no. 7893, pp. 374–379, Jan. 2022, doi: 10.1038/s41586-021-04314-4.

[55] K. Hufkens *et al.*, 'Historical Aerial Surveys Map Long-Term Changes of Forest Cover and Structure in the Central Congo Basin', *Remote Sens.*, vol. 12, no. 4, p. 638, Feb. 2020, doi: 10.3390/rs12040638.

[56] J. Nyssen *et al.*, 'Online digital archive of aerial photographs (1935–1941) of Ethiopia', *Geosci. Data J.*, vol. 9, no. 1, pp. 3–36, Jun. 2022, doi: 10.1002/gdj3.115.

[57] M. G. Burnett, 'Hexagon (KH-9) Mapping Camera Program and Evolution', National Reconnaissance Office, 1982.

[58] G. D. Krebs, 'KH-1 Corona', Gunter's Space Page. Accessed: Oct. 16, 2024. [Online]. Available: https://space.skyrocket.de/doc_sdat/kh-1.htm

[59] USGS, 'EarthExplorer'. Accessed: Oct. 16, 2024. [Online]. Available: https://earthexplorer.usgs.gov/

[60] M. J. F. Fowler, 'Declassified Intelligence Satellite Photographs', in *Archaeology from Historical Aerial and Satellite Archives*, W. S. Hanson and I. A. Oltean, Eds., New York, NY: Springer New York, 2013, pp. 47–66. doi: 10.1007/978-1-4614-4505-0_4.

[61] V. A. Piskulin, 'Economic relations of the all-union trade association Sojuzkarta and the geodetic and cartographic services of the U.S.S.R. to foreign countries', *Int. J. Remote Sens.*, vol. 10, no. 2, pp. 319–332, Feb. 1989, doi: 10.1080/01431168908903871.

[62] P. Aplin, P. M. Atkinson, and P. J. Curran, 'Fine spatial resolution satellite sensors for the next decade', *Int. J. Remote Sens.*, vol. 18, no. 18, pp. 3873–3881, Dec. 1997, doi: 10.1080/014311697216694.

[63] Defense Mapping Agency, 'Report on the Evaluation and Procurement of Former Soviet Union Imagery and Materials', 1994. Accessed: Sep. 01, 2022. [Online]. Available: https://nsarchive2.gwu.edu/NSAEBB/NSAEBB404/docs/11.pdf

[64] V. N. Lavrov, 'Space survey photocameras for cartographic purposes', in *The International Archives of the Photogrammetry, Remote Sensing and Spatial Information Sciences*, Vienna, Austria, 1996, pp. 105–109. [Online]. Available: https://www.isprs.org/proceedings/XXXI/congress/part1/

[65] V. Liebig, 'New Satellite Data with High Ground Resolution from the Space Complex MIR and Other Platforms (IP)', in *The International Archives of the Photogrammetry, Remote Sensing and Spatial Information Sciences*, Washington, D.C., 1992, pp. 167–171.

[66] V. Gupta, 'New Satellite Images for Sale', *Int. Secur.*, vol. 20, no. 1, pp. 94–125, 1995, doi: 10.2307/2539219.

[67] R. Kostka and A. Sharov, 'Geometric processing of Priroda MK-4 spaceborne multispectral images', in *Digital Photogrammetry and Remote Sensing '95*, SPIE, Dec. 1995, pp. 131–142. doi: 10.1117/12.227859.

[68] K. Torlegård, 'Sensors for photogrammetric mapping: review and prospects', *ISPRS J. Photogramm. Remote Sens.*, vol. 47, no. 4, pp. 241–262, Jun. 1992, doi: 10.1016/0924-2716(92)90017-4.

[69] M. Schmidt, R. Goossens, G. Menz, A. Altmaier, and D. Devriendt, 'The use of CORONA satellite images for generating a high resolution digital elevation model', in *IGARSS 2001. Scanning the Present and Resolving the Future. Proceedings. IEEE 2001 International Geoscience and Remote Sensing Symposium (Cat. No.01CH37217)*, Sydney, NSW, Australia: IEEE, 2001, pp. 3123–3125. doi: 10.1109/IGARSS.2001.978277.

[70] A. A. Bjørk *et al.*, 'An aerial view of 80 years of climate-related glacier fluctuations in southeast Greenland', *Nat. Geosci.*, vol. 5, no. 6, pp. 427–432, Jun. 2012, doi: 10.1038/ngeo1481.

[71] C. Sevara, 'Top Secret Topographies: Recovering Two and Three-Dimensional Archaeological Information from Historic Reconnaissance Datasets Using Image-Based Modelling Techniques', *Int. J. Herit. Digit. Era*, vol. 2, no. 3, pp. 395–418, Sep. 2013, doi: 10.1260/2047-4970.2.3.395.

[72] J. M. C. Belart, E. Magnússon, E. Berthier, F. Pálsson, Gu. Aðalgeirsdóttir, and T. Jóhannesson, 'The geodetic mass balance of Eyjafjallajökull ice cap for 1945–2014: processing guidelines and relation to climate', *J. Glaciol.*, vol. 65, no. 251, pp. 395–409, Jun. 2019, doi: 10.1017/jog.2019.16.

[73] M. W. Ewertowski, D. J. A. Evans, D. H. Roberts, A. M. Tomczyk, W. Ewertowski, and K. Pleksot, 'Quantification of historical landscape change on the foreland of a receding polythermal glacier, Hørbyebreen, Svalbard', *Geomorphology*, vol. 325, pp. 40–54, Jan. 2019, doi: 10.1016/j.geomorph.2018.09.027.

[74] O. King *et al.*, 'Six Decades of Glacier Mass Changes around Mt. Everest Are Revealed by Historical and Contemporary Images', *One Earth*, vol. 3, no. 5, pp. 608–620, 2020, doi: 10.1016/j.oneear.2020.10.019.

[75] A. Kääb *et al.*, 'Inventory and changes of rock glacier creep speeds in Ile Alatau and Kungöy Ala-Too, northern Tien Shan, since the 1950s', *The Cryosphere*, vol. 15, no. 2, pp. 927–949, Feb. 2021, doi: 10.5194/tc-15-927-2021.

[76] B. Lauzon, L. Copland, W. Van Wychen, W. Kochtitzky, R. McNabb, and D. Dahl-Jensen, 'Dynamics throughout a complete surge of Iceberg Glacier on western Axel Heiberg Island, Canadian High Arctic', *J. Glaciol.*, pp. 1–18, Apr. 2023, doi: 10.1017/jog.2023.20.

[77] B. Lauzon, L. Copland, W. Van Wychen, W. Kochtitzky, and R. McNabb, 'Evolution of the dynamics of Airdrop Glacier, western Axel Heiberg Island, over a seven decade long advance', *Arct. Sci.*, Aug. 2023, doi: 10.1139/AS-2022-0045.

[78] L. M. Andreassen, H. Elvehøy, B. Kjøllmoen, and J. M. C. Belart, 'Glacier change in Norway since the 1960s - An overview of mass balance, area, length and surface elevation changes', *J. Glaciol.*, vol. 66, no. 256, pp. 313–328, 2020, doi: 10.1017/jog.2020.10.

[79] J. M. C. Belart *et al.*, 'Mass Balance of 14 Icelandic Glaciers, 1945–2017: Spatial Variations and Links With Climate', *Front. Earth Sci.*, vol. 8, p. 163, Jun. 2020, doi: 10.3389/feart.2020.00163.

[80] D. Falaschi, M. G. Lenzano, R. Villalba, T. Bolch, A. Rivera, and A. Lo Vecchio, 'Six Decades (1958–2018) of Geodetic Glacier Mass Balance in Monte San Lorenzo, Patagonian Andes', *Front. Earth Sci.*, vol. 7, p. 326, Dec. 2019, doi: 10.3389/feart.2019.00326.

[81] L. Girod, N. I. Nielsen, F. Couderette, C. Nuth, and A. Kääb, 'Precise DEM extraction from Svalbard using 1936 high oblique imagery', *Geosci. Instrum. Methods Data Syst.*, vol. 7, no. 4, pp. 277–288, Oct. 2018, doi: 10.5194/gi-7-277-2018.

[82] T. Bolch, T. Pieczonka, and D. I. Benn, 'Multi-decadal mass loss of glaciers in the Everest area (Nepal Himalaya) derived from stereo imagery', *The Cryosphere*, vol. 5, no. 2, pp. 349–358, Apr. 2011, doi: 10.5194/tc-5-349-2011.

[83] D. Lamsal, T. Sawagaki, T. Watanabe, A. C. Byers, and D. C. McKinney, 'An assessment of conditions before and after the 1998 Tam Pokhari outburst in the Nepal Himalaya and an evaluation of the future outburst hazard: Photogrammetric Analysis of Tam Pokhari Before and After its Outburst', *Hydrol. Process.*, vol. 30, no. 5, pp. 676–691, Feb. 2016, doi: 10.1002/hyp.10636.

[84] E. Schwat, E. Istanbulluoglu, A. Horner-Devine, S. Anderson, F. Knuth, and D. Shean, 'Multi-decadal erosion rates from glacierized watersheds on Mount Baker, Washington, USA, reveal topographic, climatic, and lithologic controls on sediment yields', *Geomorphology*, vol. 438, p. 108805, Oct. 2023, doi: 10.1016/j.geomorph.2023.108805.

[85] S. N. Lane *et al.*, 'Quantification of braided river channel change using archival digital image analysis', *Earth Surf. Process. Landf.*, vol. 35, no. 8, pp. 971–985, Apr. 2010, doi: 10.1002/esp.2015.

[86] L. Piermattei *et al.*, 'Evolution of an Alpine proglacial river during 7 decades of deglaciation', *Earth Surf. Dyn.*, vol. 11, no. 3, pp. 383–403, May 2023, doi: 10.5194/esurf-11-383-2023.

[87] M. Altmann *et al.*, 'Long-Term Changes of Morphodynamics on Little Ice Age Lateral Moraines and the Resulting Sediment Transfer into Mountain Streams in the Upper Kauner Valley, Austria', *Water*, vol. 12, no. 12, p. 3375, Dec. 2020, doi: 10.3390/w12123375.

[88] M. Llena, D. Vericat, M. Cavalli, S. Crema, and M. W. Smith, 'The effects of land use and topographic changes on sediment connectivity in mountain catchments', *Sci. Total Environ.*, vol. 660, pp. 899–912, Apr. 2019, doi: 10.1016/j.scitotenv.2018.12.479.

[89] A. Casado, B. Hortobágyi, and E. Roussel, 'Historic reconstruction of reservoir topography using contour line interpolation and structure from motion photogrammetry', *Int. J. Geogr. Inf. Sci.*, vol. 32, no. 12, pp. 2427–2446, Dec. 2018, doi: 10.1080/13658816.2018.1511795.

[90] J. Cardenal, J. Delgado, E. Mata, A. González, and I. Olague, 'Use of historical flight for landslide monitoring', in *Proceedings of the Spatial Accuracy 2006*, Lisbonne, Portugal, 2006, pp. 129–138.

[91] M. Del Soldato *et al.*, 'Multisource data integration to investigate one century of evolution for the Agnone landslide (Molise, southern Italy)', *Landslides*, vol. 15, no. 11, pp. 2113–2128, Nov. 2018, doi: 10.1007/s10346-018-1015-z.

[92] J. A. Warrick, A. C. Ritchie, G. Adelman, K. Adelman, and P. W. Limber, 'New Techniques to Measure Cliff Change from Historical Oblique Aerial Photographs and Structure-from-Motion Photogrammetry', *J. Coast. Res.*, vol. 33, no. 1, p. 39, Jan. 2017, doi: 10.2112/JCOASTRES-D-16-00095.1.

[93] J. Aga *et al.*, 'Acceleration of coastal-retreat rates for high-Arctic rock cliffs on Brøggerhalvøya, Svalbard, over the past decade', *Earth Surf. Dyn.*, vol. 12, no. 5, pp. 1049–1070, Sep. 2024, doi: 10.5194/esurf-12-1049-2024.

[94] B. Stichelbaut and J. Bourgeois, 'The Aerial Imagery of World War One: A Unique Source for Conflict and Landscape Archaeology', *Photogramm. - Fernerkund.*

- *Geoinformation*, vol. 2009, no. 3, pp. 235–244, Jul. 2009, doi: 10.1127/0935-1221/2009/0018.

[95] A. V. Shevchenko *et al.*, 'The rebirth and evolution of Bezymianny volcano, Kamchatka after the 1956 sector collapse', *Commun. Earth Environ.*, vol. 1, no. 1, pp. 1–15, 2020, doi: 10.1038/s43247-020-00014-5.

[96] N. J. Korsgaard *et al.*, 'Digital elevation model and orthophotographs of Greenland based on aerial photographs from 1978–1987', *Sci. Data*, vol. 3, no. 1, p. 160032, Dec. 2016, doi: 10.1038/sdata.2016.32.

[97] H. Heisig and J.-L. Simmen, 'Re-engineering the Past: Countrywide Geo-referencing of Archival Aerial Imagery', *PFG – J. Photogramm. Remote Sens. Geoinformation Sci.*, vol. 89, no. 6, pp. 487–503, Dec. 2021, doi: 10.1007/s41064-021-00162-z.

[98] A. Dashora, B. Lohani, and J. N. Malik, 'A repository of earth resource information – CORONA satellite programme', *Curr. Sci.*, vol. 92, no. 7, pp. 926–932, 2007.

[99] H. Papworth, A. Ford, K. Welham, and D. Thackray, 'Assessing 3D metric data of digital surface models for extracting archaeological data from archive stereo-aerial photographs', *J. Archaeol. Sci.*, vol. 72, pp. 85–104, Aug. 2016, doi: 10.1016/j.jas.2016.05.005.

[100] J. Walstra, J. Chandler, N. Dixon, and T. Dijkstra, 'Time for change: quantifying landslide evolution using historical aerial photographs and modern photogrammetric methods', in *The International Archives of the Photogrammetry, Remote Sensing and Spatial Information Sciences*, Istanbul, Turkey: International Society for Photogrammetry and Remote Sensing (ISPRS). Commission IV. Working Group 8, 2004, pp. 475–480. Accessed: Mar. 22, 2021. [Online]. Available: http://hdl.handle.net/1854/LU-365820

[101] D. Zawieska, J. Markiewicz, and J. Kopiasz, 'Development of true orthophotomaps of the fortified settlement at Biskupin, Site 4, based on archival data', *Archaeol. Prospect.*, vol. 26, no. 4, pp. 333–360, Oct. 2019, doi: 10.1002/arp.1748.

[102] Y. Tian, M. Xia, X. Li, G. Qiao, and R. Li, 'Applications of Historical Optical DISP Images in Antarctica Study', in *IGARSS 2019 - 2019 IEEE International Geoscience and Remote Sensing Symposium*, Yokohama, Japan: IEEE, Jul. 2019, pp. 3994–3997. doi: 10.1109/IGARSS.2019.8900380.

[103] R. Li *et al.*, 'A New Analytical Method for Estimating Antarctic Ice Flow in the 1960s From Historical Optical Satellite Imagery', *IEEE Trans. Geosci. Remote Sens.*, vol. 55, no. 5, pp. 2771–2785, May 2017, doi: 10.1109/TGRS.2017.2654484.

[104] E. M. Mikhail, J. S. Bethel, J. C. MacGlone, and J. C. McGlone, *Introduction to modern photogrammetry*. New York Chichester Weinheim: Wiley, 2001.

[105] P. R. Wolf and B. A. Dewitt, *Elements of photogrammetry: with applications in GIS*, 3rd. ed. New York: McGraw-Hill, 2000.

[106] K. Kraus, I. Harley, and K. Kraus, *Photogrammetry: geometry from images and laser scans*, 2. ed. in De Gruyter Textbook. Berlin: de Gruyter, 2007. doi: 10.1515/9783110892871.

[107] W. Förstner and B. P. Wrobel, *Photogrammetric Computer Vision*, vol. 11. in Geometry and Computing, vol. 11. Cham: Springer International Publishing, 2016. doi: 10.1007/978-3-319-11550-4.

[108] F. Knuth *et al.*, 'Historical Structure from Motion (HSfM): Automated processing of historical aerial photographs for long-term topographic change analysis', *Remote Sens. Environ.*, vol. 285, p. 113379, 2023, doi: 10.1016/j.rse.2022.113379.

[109] R. McNabb, *spymicmac*. (Jun. 05, 2025). Zenodo. doi: 10.5281/ZENODO.15602812.

[110] T. Pieczonka, T. Bolch, W. Junfeng, and L. Shiyin, 'Heterogeneous mass loss of glaciers in the Aksu-Tarim Catchment (Central Tien Shan) revealed by 1976 KH-9 Hexagon and 2009 SPOT-5 stereo imagery', *Remote Sens. Environ.*, vol. 130, pp. 233–244, 2013, doi: 10.1016/j.rse.2012.11.020.

[111] S. F. Child, L. A. Stearns, L. Girod, and H. H. Brecher, 'Structure-from-motion photogrammetry of Antarctic historical aerial photographs in conjunction with ground control derived from satellite data', *Remote Sens.*, vol. 13, no. 1, pp. 1–25, 2021, doi: 10.3390/rs13010021.

[112] T. Bolch, T. Pieczonka, K. Mukherjee, and J. Shea, 'Brief communication: Glaciers in the Hunza catchment (Karakoram) have been nearly in balance since the 1970s', *The Cryosphere*, vol. 11, no. 1, pp. 531–539, Feb. 2017, doi: 10.5194/tc-11-531-2017.

[113] T. Pieczonka and T. Bolch, 'Region-wide glacier mass budgets and area changes for the Central Tien Shan between ~ 1975 and 1999 using Hexagon KH-9 imagery', *Glob. Planet. Change*, vol. 128, pp. 1–13, 2015, doi: 10.1016/j.gloplacha.2014.11.014.

[114] J. Maurer and S. Rupper, 'Tapping into the Hexagon spy imagery database: A new automated pipeline for geomorphic change detection', *ISPRS J. Photogramm. Remote Sens.*, vol. 108, pp. 113–127, Oct. 2015, doi: 10.1016/j.isprsjprs.2015.06.008.

[115] Z. Rendenieks, M. D. Nita, O. Nikodemus, and V. C. Radeloff, 'Half a century of forest cover change along the Latvian-Russian border captured by object-based image analysis of Corona and Landsat TM/OLI data', *Remote Sens. Environ.*, vol. 249, p. 112010, Nov. 2020, doi: 10.1016/j.rse.2020.112010.

[116] S. Ghuffar, O. King, G. Guillet, E. Rupnik, and T. Bolch, 'Brief communication: Glacier mapping and change estimation using very high-resolution declassified Hexagon KH-9 panoramic stereo imagery (1971–1984)', *The Cryosphere*, vol. 17, no. 3, pp. 1299–1306, Mar. 2023, doi: 10.5194/tc-17-1299-2023.

[117] C. Sevara, G. Verhoeven, M. Doneus, and E. Draganits, 'Surfaces from the Visual Past: Recovering High-Resolution Terrain Data from Historic Aerial Imagery for Multitemporal Landscape Analysis', *J. Archaeol. Method Theory*, vol. 25, no. 2, pp. 611–642, Jun. 2018, doi: 10.1007/s10816-017-9348-9.

[118] J. R. Mertes, J. D. Gulley, D. I. Benn, S. S. Thompson, and L. I. Nicholson, 'Using structure-from-motion to create glacier DEMs and orthoimagery from historical terrestrial and oblique aerial imagery: SfM on Differing

Historical Glacier Imagery Sets', *Earth Surf. Process. Landf.*, vol. 42, no. 14, pp. 2350–2364, Nov. 2017, doi: 10.1002/esp.4188.

[119] I. Picon-Cabrera, J. M. Garcia-Gago, L. J. Sanchez-Aparicio, P. Rodriguez-Gonzalvez, and D. Gonzalez-Aguilera, 'On the Use of Historical Flights for the Urban Growth Analysis of Cities Through Time: The Case Study of Avila (Spain)', *Sustainability*, vol. 12, no. 11, p. 4673, Jun. 2020, doi: 10.3390/su12114673.

[120] K. C. Bolles and S. L. Forman, 'Evaluating Landscape Degradation Along Climatic Gradients During the 1930s Dust Bowl Drought From Panchromatic Historical Aerial Photographs, United States Great Plains', *Front. Earth Sci.*, vol. 6, p. 153, Oct. 2018, doi: 10.3389/feart.2018.00153.

[121] A. Frankl, V. Seghers, C. Stal, P. De Maeyer, G. Petrie, and J. Nyssen, 'Using image-based modelling (SfM–MVS) to produce a 1935 ortho-mosaic of the Ethiopian highlands', *Int. J. Digit. Earth*, vol. 8, no. 5, pp. 421–430, May 2015, doi: 10.1080/17538947.2014.942715.

[122] E. Grottoli, M. Biausque, D. Rogers, D. W. T. Jackson, and J. A. G. Cooper, 'Structure-from-Motion-Derived Digital Surface Models from Historical Aerial Photographs: A New 3D Application for Coastal Dune Monitoring', *Remote Sens.*, vol. 13, no. 1, p. 95, 2021, doi: 10.3390/rs13010095.

[123] M. Vastaranta *et al.*, 'Forest stand age classification using time series of photogrammetrically derived digital surface models', *Scand. J. For. Res.*, vol. 31, no. 2, pp. 194–205, 2015, doi: 10.1080/02827581.2015.1060256.

[124] A. T. Pinto, J. A. Gonçalves, P. Beja, and J. Pradinho Honrado, 'From Archived Historical Aerial Imagery to Informative Orthophotos: A Framework for Retrieving the Past in Long-Term Socioecological Research', *Remote Sens.*, vol. 11, no. 11, p. 1388, Jun. 2019, doi: 10.3390/rs11111388.

[125] P. Bożek, J. Janus, and B. Mitka, 'Analysis of Changes in Forest Structure using Point Clouds from Historical Aerial Photographs', *Remote Sens.*, vol. 11, no. 19, p. 2259, Sep. 2019, doi: 10.3390/rs11192259.

[126] F. Fleischer *et al.*, 'Multi-decadal (1953–2017) rock glacier kinematics analysed by high-resolution topographic data in the upper Kaunertal, Austria', *The Cryosphere*, vol. 15, no. 12, pp. 5345–5369, Dec. 2021, doi: 10.5194/tc-15-5345-2021.

[127] E. Magnússon, J. M.-C. Belart, F. Pálsson, H. Ágústsson, and P. Crochet, 'Geodetic mass balance record with rigorous uncertainty estimates deduced from aerial photographs and lidar data – Case study from Drangajökull ice cap, NW Iceland', *The Cryosphere*, p. 19, 2016, doi: 10.5194/tc-10-159-2016.

[128] X. Hong and C. H. Roosevelt, 'Orthorectification of Large Datasets of Multi-scale Archival Aerial Imagery: A Case Study from Türkiye', *J. Geovisualization Spat. Anal.*, vol. 7, no. 2, p. 23, Dec. 2023, doi: 10.1007/s41651-023-00153-1.

[129] C. Mestre-Runge, J. Lorenzo-Lacruz, A. Ortega-Mclear, and C. Garcia, 'An Optimized Workflow for Digital Surface Model Series Generation Based on Historical Aerial Images: Testing and Quality Assessment in the Beach-Dune System of Sa Ràpita-Es Trenc (Mallorca, Spain)', *Remote Sens.*, vol. 15, no. 8, p. 2044, Apr. 2023, doi: 10.3390/rs15082044.

[130] E. Rupnik, M. Daakir, and M. Pierrot Deseilligny, 'MicMac – a free, open-source solution for photogrammetry', *Open Geospatial Data Softw. Stand.*, vol. 2, no. 1, p. 14, Dec. 2017, doi: 10.1186/s40965-017-0027-2.

[131] E. S. Holmlund, 'Aldegondabreen glacier change since 1910 from structure-from-motion photogrammetry of archived terrestrial and aerial photographs: utility of a historic archive to obtain century-scale Svalbard glacier mass losses', *J. Glaciol.*, vol. 67, no. 261, pp. 107–116, Feb. 2021, doi: 10.1017/jog.2020.89.

[132] M. A. Núñez-Andrés, F. Buill, M. Hürlimann, and C. Abancó, 'Multi-temporal analysis of morphologic changes applying geomatic techniques. 70 years of torrential activity in the Rebaixader catchment (Central pyrenees)', *Geomat. Nat. Hazards Risk*, vol. 10, no. 1, pp. 314–335, Jan. 2019, doi: 10.1080/19475705.2018.1523235.

[133] P. T. Stăncioiu, M. D. Niță, and M. Fedorca, 'Capercaillie (Tetrao urogallus) habitat in Romania – A landscape perspective revealed by Cold War spy satellite images', *Sci. Total Environ.*, vol. 781, p. 146763, Aug. 2021, doi: 10.1016/j.scitotenv.2021.146763.

[134] N. Mölg and T. Bolch, 'Structure-from-Motion Using Historical Aerial Images to Analyse Changes in Glacier Surface Elevation', *Remote Sens.*, vol. 9, no. 10, p. 1021, Oct. 2017, doi: 10.3390/rs9101021.

[135] P. Kupidura, K. Osińska-Skotak, K. Lesisz, and A. Podkowa, 'The Efficacy Analysis of Determining the Wooded and Shrubbed Area Based on Archival Aerial Imagery Using Texture Analysis', *ISPRS Int. J. Geo-Inf.*, vol. 8, no. 10, Art. no. 10, Oct. 2019, doi: 10.3390/ijgi8100450.

[136] A. Bhattacharya *et al.*, 'High Mountain Asian glacier response to climate revealed by multi-temporal satellite observations since the 1960s', *Nat. Commun.*, vol. 12, no. 1, p. 4133, Dec. 2021, doi: 10.1038/s41467-021-24180-y.

[137] N. Galiatsatos, D. N. M. Donoghue, and G. Philip, 'High resolution elevation data derived from stereoscopic CORONA imagery with minimal ground control: An approach using Ikonos and SRTM data', *Photogramm. Eng. Remote Sens.*, vol. 74, no. 9, pp. 1093–1106, 2008, doi: 10.14358/PERS.74.9.1093.

[138] B. A. Robson, C. Nuth, P. R. Nielsen, L. Girod, M. Hendrickx, and S. O. Dahl, 'Spatial Variability in Patterns of Glacier Change across the Manaslu Range, Central Himalaya', *Front. Earth Sci.*, vol. 6, no. February, pp. 1–19, 2018, doi: 10.3389/feart.2018.00012.

[139] Z. Hou *et al.*, '2OC: A General Automated Orientation and Orthorectification Method for Corona KH-4B Panoramic Imagery', *Remote Sens.*, vol. 15, no. 21, p. 5116, Oct. 2023, doi: 10.3390/rs15215116.

[140] A. Surazakov and V. Aizen, ‘Positional Accuracy Evaluation of Declassified Hexagon KH-9 Mapping Camera Imagery’, *Photogramm. Eng. Remote Sens.*, vol. 76, no. 5, pp. 603–608, May 2010, doi: 10.14358/PERS.76.5.603.

[141] R. A. Beyer, O. Alexandrov, and S. McMichael, ‘The Ames Stereo Pipeline: NASA’s open source software for deriving and processing terrain data’, *Earth Space Sci.*, vol. 5, no. 9, pp. 537–548, 2018, doi: 10.1029/2018EA000409.

[142] P. Lacroix, A. Dehecq, and E. Taipe, ‘Irrigation-triggered landslides in a Peruvian desert caused by modern intensive farming’, *Nat. Geosci.*, vol. 13, no. 1, pp. 56–60, Jan. 2020, doi: 10.1038/s41561-019-0500-x.

[143] M. Persia, E. Barca, R. Greco, M. I. Marzulli, and P. Tartarino, ‘Archival Aerial Images Georeferencing: A Geostatistically-Based Approach for Improving Orthophoto Accuracy with Minimal Number of Ground Control Points’, *Remote Sens.*, vol. 12, no. 14, p. 2232, Jul. 2020, doi: 10.3390/rs12142232.

[144] J. G. Fryer and H. L. Mitchell, ‘Radial distortion and close-range stereophotogrammetry’, *Aust. J. Geod. Photogramm. Surv.*, vol. 46 and 47, pp. 123–138, 1987.

[145] M. R. James and S. Robson, ‘Mitigating systematic error in topographic models derived from UAV and ground-based image networks’, *Earth Surf. Process. Landf.*, vol. 39, no. 10, pp. 1413–1420, Aug. 2014, doi: 10.1002/esp.3609.

[146] R. Wackrow and J. H. Chandler, ‘A convergent image configuration for DEM extraction that minimises the systematic effects caused by an inaccurate lens model’, *Photogramm. Rec.*, vol. 23, no. 121, pp. 6–18, Mar. 2008, doi: 10.1111/j.1477-9730.2008.00467.x.

[147] K. Schwidefsky and F. Ackermann, *Photogrammetrie: Grundlagen, Verfahren, Anwendungen*, 7., Neubearbeitete und erweiterte Auflage. Wiesbaden: Vieweg+Teubner Verlag, 1976. doi: 10.1007/978-3-322-94008-7.

[148] L. Zhang, E. Rupnik, and M. Pierrot-Deseilligny, ‘Feature matching for multi-epoch historical aerial images’, *ISPRS J. Photogramm. Remote Sens.*, vol. 182, pp. 176–189, Dec. 2021, doi: 10.1016/j.isprsjprs.2021.10.008.

[149] M. Bakker and S. N. Lane, ‘Archival photogrammetric analysis of river-floodplain systems using Structure from Motion (SfM) methods: Archival Photogrammetric Analysis of River Systems using SfM Methods’, *Earth Surf. Process. Landf.*, vol. 42, no. 8, pp. 1274–1286, Jun. 2017, doi: 10.1002/esp.4085.

[150] S. N. Lane, S. C. Reid, R. M. Westaway, and D. M. Hicks, ‘Remotely Sensed Topographic Data for River Channel Research: The Identification, Explanation and Management of Error’, in *Spatial Modelling of the Terrestrial Environment*, John Wiley & Sons, Ltd, 2004, pp. 113–136. doi: 10.1002/0470094001.ch6.

[151] M. A. Fonstad, J. T. Dietrich, B. C. Courville, J. L. Jensen, and P. E. Carbonneau, ‘Topographic structure from motion: a new development in photogrammetric measurement’, *Earth Surf. Process. Landf.*, vol. 38, no. 4, pp. 421–430, Mar. 2013, doi: 10.1002/esp.3366.

[152] L. J. Lajoie, E. Nissen, K. L. Johnson, and K. R. Lajoie, ‘Submeter Resolution Surface Rupture Topography From Legacy Aerial Photographs—A Test Case From the 1992 Landers Earthquake’, *Earth Space Sci.*, vol. 7, no. 3, Mar. 2020, doi: 10.1029/2019EA000651.

[153] A. Bhattacharya, S. Ghosh, and K. Mukherjee, ‘Multi-decadal mass budget and area change of some eastern Himalayan glaciers (Nepal-Sikkim) using remote sensing techniques’, in *2018 4th International Conference on Recent Advances in Information Technology (RAIT)*, Dhanbad: IEEE, Mar. 2018, pp. 1–6. doi: 10.1109/RAIT.2018.8388976.

[154] Y. Zhou, Z. Li, J. Li, R. Zhao, and X. Ding, ‘Geodetic glacier mass balance (1975–1999) in the central Pamir using the SRTM DEM and KH-9 imagery’, *J. Glaciol.*, vol. 65, no. 250, pp. 309–320, Apr. 2019, doi: 10.1017/jog.2019.8.

[155] M. Llena, M. Cavalli, D. Vericat, and S. Crema, ‘Assessing landscape changes associated to anthropic disturbances by means of the application of Structure from Motion photogrammetry using historical aerial imagery’, *Rendiconti Online Della Soc. Geol. Ital.*, vol. 46, pp. 74–81, Nov. 2018, doi: 10.3301/ROL.2018.55.

[156] M. V. Peppa *et al.*, ‘Archaeological Feature Detection from Archive Aerial Photography with a Sfm-Mvs and Image Enhancement Pipeline’, in *The International Archives of the Photogrammetry, Remote Sensing and Spatial Information Sciences*, Riva del Garda, Italy, May 2018, pp. 869–875. doi: 10.5194/isprs-archives-XLII-2-869-2018.

[157] C. Ressl, G. Mandlburger, and N. Pfeifer, ‘Investigating adjustment of Airborne Laser Scanning strips without usage of GNSS/IMU trajectory data’, in *ISPRS Archives – Volume XXXVIII-3/W8*, Paris, France, 2009, pp. 195–200. Accessed: Jan. 03, 2025. [Online]. Available: https://www.isprs.org/proceedings/xxxviii/3-w8/papers/195_laserscanning09.pdf

[158] C. Nuth and A. Kääb, ‘Co-registration and bias corrections of satellite elevation data sets for quantifying glacier thickness change’, *The Cryosphere*, vol. 5, no. 1, pp. 271–290, Mar. 2011, doi: 10.5194/tc-5-271-2011.

[159] D. Shean *et al.*, *dshean/demcoreg: v1.1.1 Compatibility and doc improvements*. (Mar. 13, 2023). Zenodo. doi: 10.5281/ZENODO.3243480.

[160] xDEM contributors, *xDEM*. (2024). Zenodo. doi: 10.5281/zenodo.11492983.

[161] T. Li, Y. Hu, B. Liu, L. Jiang, H. Wang, and X. Shen, ‘Co-registration and residual correction of digital elevation models: a comparative study’, *The Cryosphere*, vol. 17, no. 12, pp. 5299–5316, Dec. 2023, doi: 10.5194/tc-17-5299-2023.

[162] D. Lague, N. Brodu, and J. Leroux, ‘Accurate 3D comparison of complex topography with terrestrial laser scanner: Application to the Rangitikei canyon (N-Z)’, *ISPRS J. Photogramm. Remote Sens.*, vol. 82, pp. 10–26, Aug. 2013, doi: 10.1016/j.isprsjprs.2013.04.009.

[163] B. Mihai, C. Nistor, L. Toma, and I. Săvulescu, 'High Resolution Landscape Change Analysis with CORONA KH-4B Imagery. A Case Study from Iron Gates Reservoir Area', *Procedia Environ. Sci.*, vol. 32, pp. 200–210, 2016, doi: 10.1016/j.proenv.2016.03.025.

[164] G. Pulighe and F. Fava, 'DEM extraction from archive aerial photos: accuracy assessment in areas of complex topography', *Eur. J. Remote Sens.*, vol. 46, no. 1, pp. 363–378, Jan. 2013, doi: 10.5721/EuJRS20134621.

[165] D. Girardeau-Montaut, *CloudCompare*. (2019). [Online]. Available: https://cloudcompare.org/

[166] D. Farías-Barahona *et al.*, 'A near 90-year record of the evolution of El Morado Glacier and its proglacial lake, Central Chilean Andes', *J. Glaciol.*, vol. 66, no. 259, pp. 846–860, Oct. 2020, doi: 10.1017/jog.2020.52.

[167] B. V. Óskarsson, K. Jónasson, G. Valsson, and J. M. C. Belart, 'Erosion and sedimentation in Surtsey island quantified from new DEMs', *Surtsey Res.*, vol. 14, pp. 63–77, 2020, doi: 10.33112/surtsey.14.5.

[168] R. W. McNabb, C. Nuth, A. M. Kääb, and L. Girod, 'Sensitivity of glacier volume change estimation to DEM void interpolation', *The Cryosphere*, vol. 13, no. 3, pp. 895–910, 2019, doi: 10.5194/tc-13-895-2019.

[169] S. Ishiguro, H. Yamano, and H. Oguma, 'Evaluation of DSMs generated from multi-temporal aerial photographs using emerging structure from motion–multi-view stereo technology', *Geomorphology*, vol. 268, pp. 64–71, Sep. 2016, doi: 10.1016/j.geomorph.2016.05.029.

[170] M. A. Aguilar, F. J. Aguilar, I. Fernández, and J. P. Mills, 'Accuracy Assessment of Commercial Self-Calibrating Bundle Adjustment Routines Applied to Archival Aerial Photography', *Photogramm. Rec.*, vol. 28, no. 141, pp. 96–114, Mar. 2013, doi: 10.1111/j.1477-9730.2012.00704.x.

[171] J. Walstra, J. H. Chandler, N. Dixon, and R. Wackrow, 'Evaluation of the controls affecting the quality of spatial data derived from historical aerial photographs', *Earth Surf. Process. Landf.*, vol. 36, no. 7, pp. 853–863, Jun. 2011, doi: 10.1002/esp.2111.

[172] S. Seccaroni, M. Santangelo, I. Marchesini, A. Mondini, and M. Cardinali, 'High Resolution Historical Topography: Getting More from Archival Aerial Photographs', *Proceedings*, vol. 2, no. 7, p. 347, Mar. 2018, doi: 10.3390/ecrs-2-05160.

[173] S. M. M. Kahaki, M. J. Nordin, A. H. Ashtari, and S. J. Zahra, 'Invariant Feature Matching for Image Registration Application Based on New Dissimilarity of Spatial Features', *PLOS ONE*, vol. 11, no. 3, p. e0149710, Mar. 2016, doi: 10.1371/journal.pone.0149710.

[174] E. M. Farella, L. Morelli, F. Remondino, J. P. Mills, N. Haala, and J. Crompvoets, 'The EuroSDR TIME Benchmark for historical aerial images', in *The International Archives of the Photogrammetry, Remote Sensing and Spatial Information Sciences*, Nice, France, May 2022, pp. 1175–1182. doi: 10.5194/isprs-archives-XLIII-B2-2022-1175-2022.

[175] P. Polewski and W. Yao, 'Scale invariant line-based co-registration of multimodal aerial data using L1 minimization of spatial and angular deviations', *ISPRS J. Photogramm. Remote Sens.*, vol. 152, pp. 79–93, Jun. 2019, doi: 10.1016/j.isprsjprs.2019.04.004.

[176] P.-E. Sarlin, D. DeTone, T. Malisiewicz, and A. Rabinovich, 'SuperGlue: Learning Feature Matching With Graph Neural Networks', in *2020 IEEE/CVF Conference on Computer Vision and Pattern Recognition (CVPR)*, Jun. 2020, pp. 4937–4946. doi: 10.1109/CVPR42600.2020.00499.

[177] M. J. Tyszkiewicz, P. Fua, and E. Trulls, 'DISK: Learning local features with policy gradient', Oct. 27, 2020, *arXiv*: arXiv:2006.13566. doi: 10.48550/arXiv.2006.13566.

[178] F. Bellavia, L. Morelli, F. Menna, and F. Remondino, 'Image orientation with a hybrid pipeline robust to rotations and wide-baselines', *Int. Arch. Photogramm. Remote Sens. Spat. Inf. Sci.*, vol. XLVI-2/W1-2022, pp. 73–80, Feb. 2022, doi: 10.5194/isprs-archives-XLVI-2-W1-2022-73-2022.

[179] F. Remondino, L. Morelli, E. Stathopoulou, M. Elhashash, and R. Qin, 'Aerial triangulation with learning-based tie points', *Int. Arch. Photogramm. Remote Sens. Spat. Inf. Sci.*, vol. XLIII-B2-2022, pp. 77–84, May 2022, doi: 10.5194/isprs-archives-XLIII-B2-2022-77-2022.

[180] F. Dahle, R. Lindenbergh, and B. Wouters, 'Revisiting the Past: A comparative study for semantic segmentation of historical images of Adelaide Island using U-nets', *ISPRS Open J. Photogramm. Remote Sens.*, vol. 11, p. 100056, Jan. 2024, doi: 10.1016/j.ophoto.2023.100056.

[181] K. L. Cook and M. Dietze, 'Short Communication: A simple workflow for robust low-cost UAV-derived change detection without ground control points', *Earth Surf. Dyn.*, vol. 7, no. 4, pp. 1009–1017, Oct. 2019, doi: 10.5194/esurf-7-1009-2019.

[182] D. Craciun and A. Le Bris, 'Automatic algorithm for georeferencing historical-to-nowadays aerial images acquired in natural environments', in *The International Archives of the Photogrammetry, Remote Sensing and Spatial Information Sciences*, Nice, France, May 2022, pp. 21–28. doi: 10.5194/isprs-archives-XLIII-B2-2022-21-2022.

[183] L. Maurya, V. Lohchab, P. Kumar Mahapatra, and J. Abonyi, 'Contrast and brightness balance in image enhancement using Cuckoo Search-optimized image fusion', *J. King Saud Univ. - Comput. Inf. Sci.*, vol. 34, no. 9, pp. 7247–7258, Oct. 2022, doi: 10.1016/j.jksuci.2021.07.008.

[184] L. Lelégard, A. Le Bris, and S. Giordano, 'Improving Local Adaptive Filtering Method Employed in Radiometric Correction of Analogue Airborne Campaigns', *Int. Arch. Photogramm. Remote Sens. Spat. Inf. Sci.*, vol. XLIII-B3-2022, pp. 1217–1222, May 2022, doi: 10.5194/isprs-archives-XLIII-B3-2022-1217-2022.

[185] I. Marzolff, M. Kirchhoff, R. Stephan, M. Seeger, A. Aït Hssaine, and J. B. Ries, 'Monitoring Dryland Trees With Remote Sensing. Part A: Beyond CORONA—Historical HEXAGON Satellite Imagery as a New Data

Source for Mapping Open-Canopy Woodlands on the Tree Level', *Front. Environ. Sci.*, vol. 10, p. 896702, Jul. 2022, doi: 10.3389/fenvs.2022.896702.

[186] A. R. Shahtahmassebi *et al.*, 'De-noised and contrast enhanced KH-9 HEXAGON mapping and panoramic camera images for urban research', *Sci. Remote Sens.*, vol. 7, p. 100082, Jun. 2023, doi: 10.1016/j.srs.2023.100082.

[187] EuroSDR, 'Benchmark TIME'. 2021. [Online]. Available: https://time.fbk.eu/

[188] Y. Jin *et al.*, 'Image Matching Across Wide Baselines: From Paper to Practice', *Int. J. Comput. Vis.*, vol. 129, no. 2, pp. 517–547, Feb. 2021, doi: 10.1007/s11263-020-01385-0.

[189] R. Hugonnet *et al.*, 'Uncertainty Analysis of Digital Elevation Models by Spatial Inference From Stable Terrain', *IEEE J. Sel. Top. Appl. Earth Obs. Remote Sens.*, vol. 15, pp. 6456–6472, 2022, doi: 10.1109/JSTARS.2022.3188922.

[190] C. P. McAuliffe, K. Lage, and R. Mattke, 'Access to Online Historical Aerial Photography Collections: Past Practice, Present State, and Future Opportunities', *J. Map Geogr. Libr.*, vol. 13, no. 2, pp. 198–221, May 2017, doi: 10.1080/15420353.2017.1334252.

[191] Swisstopo, 'Aerial photography - Federal Office of Topography swisstopo', Aerial Photographs. Accessed: Mar. 24, 2025. [Online]. Available: https://www.swisstopo.admin.ch/en/analogue-aerial-photographs

[192] S. Zhang, H. A. Barrett, S. V. Baros, P. R. H. Neville, S. Talasila, and L. L. Sinclair, 'Georeferencing Accuracy Assessment of Historical Aerial Photos Using a Custom-Built Online Georeferencing Tool', *ISPRS Int. J. Geo-Inf.*, vol. 11, no. 12, p. 582, Nov. 2022, doi: 10.3390/ijgi11120582.

[193] NRO, 'Hexagon: America's Eyes in Space', Center for the Study of National Reconnaissance, 2011.

[194] S. Bogart, 'SankeyMatic'. Accessed: Jan. 01, 2025. [Online]. Available: https://sankeymatic.com/build/

GRSM-2025-00058

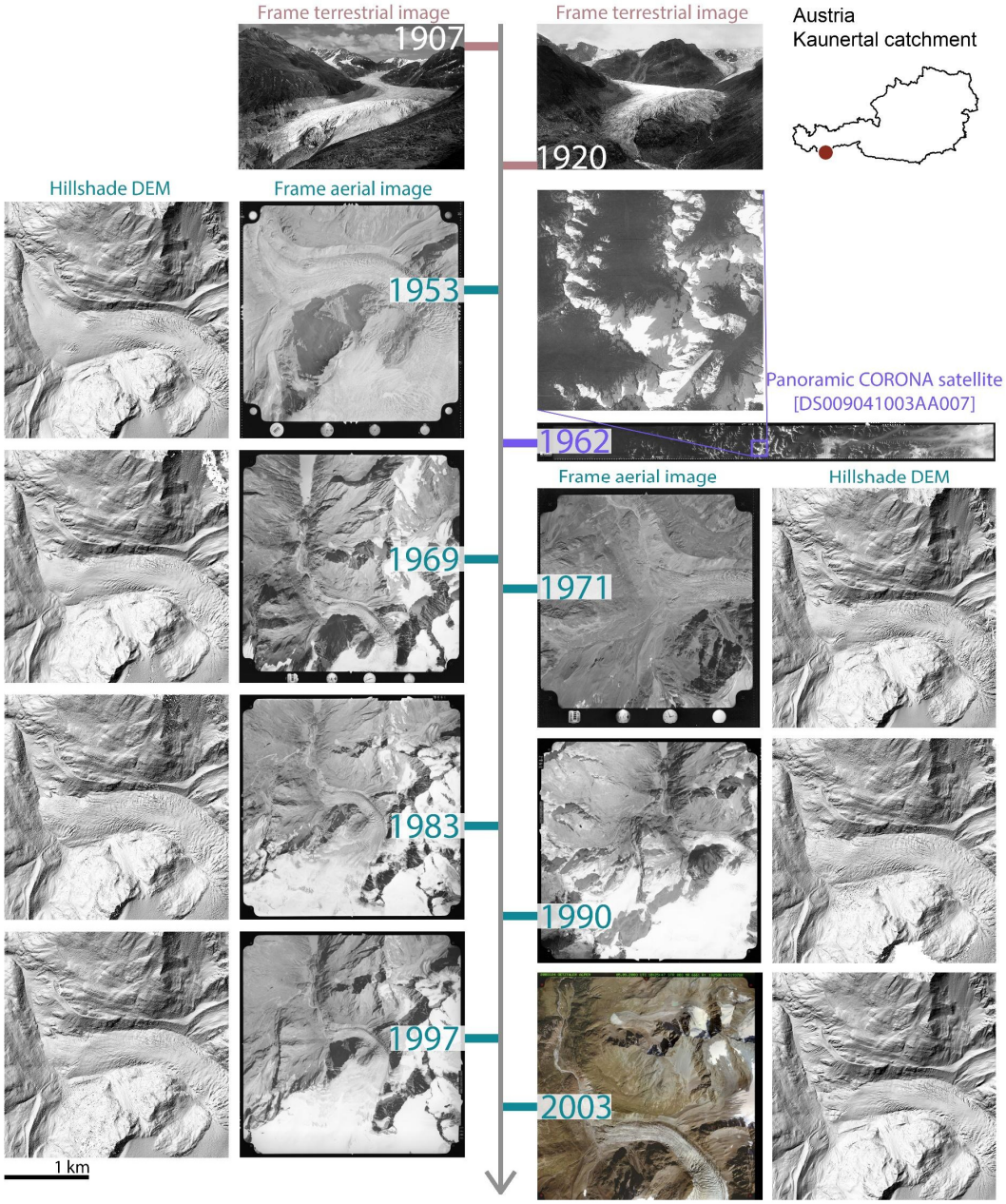

Fig. 1. A time series of terrestrial, aerial, and CORONA historical images, with derived hillshade DEMs of the Gepatch Glacier in the Kaunertal catchment, Austria. Credits: Terrestrial image from 1907: Austrian Alpine Club (ÖAV). Terrestrial image from 1920: Provided by Martin Frey; the original photographer is unknown. Aerial image: Federal Office of Metrology and Surveying (BEV) and the Province of Tyrol (Land Tirol). Hillshade produced by [86]. CORONA panoramic image: USGS.

GRSM-2025-00058

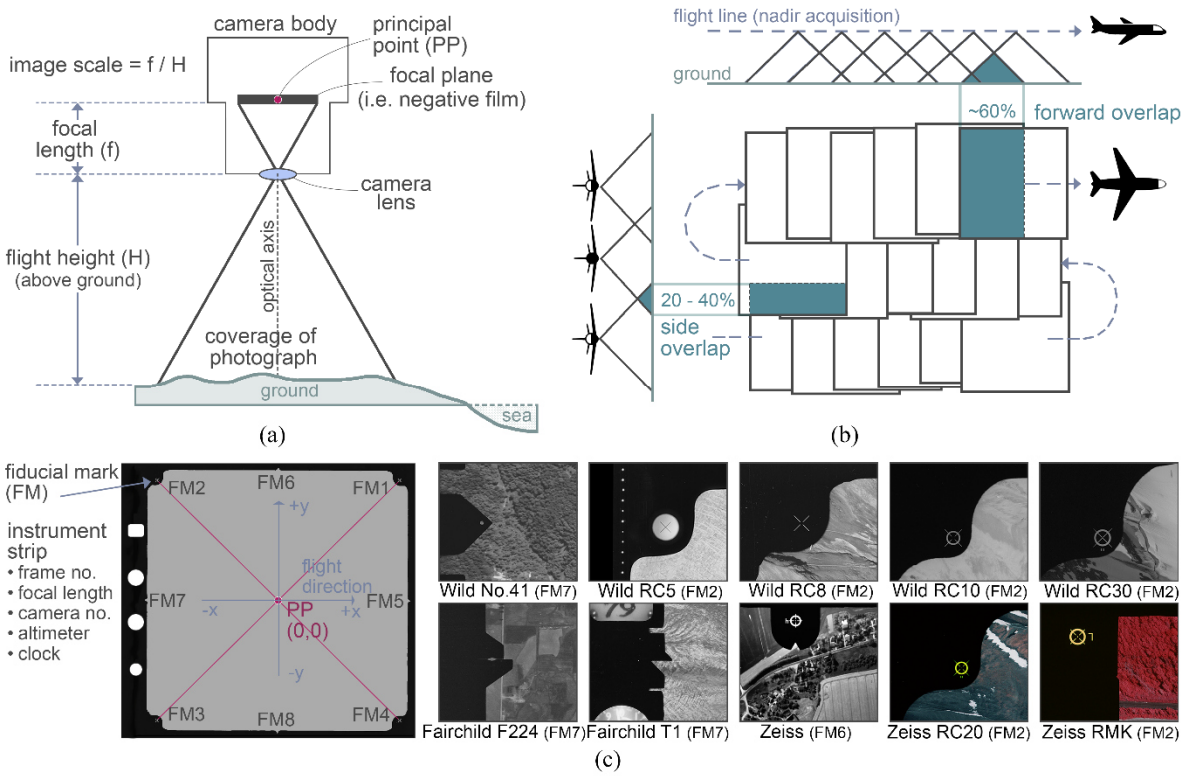

Fig. 2. Aerial frame characteristics. a) Central projection of a single image, b) illustration of the flight plan and image overlap. c) Distribution of fiducial marks and examples from different aerial cameras.

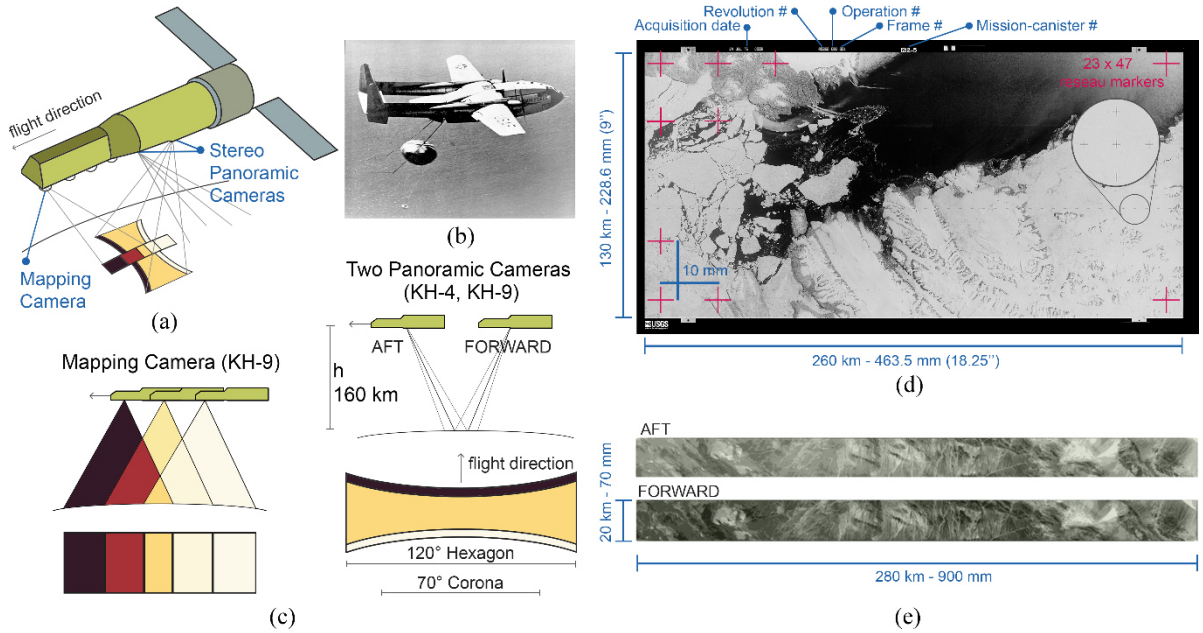

Fig. 3. a) Illustration of a Hexagon reconnaissance system. b) Mid-air Corona film recovery (Credit: U.S. Air Force). c) An illustration of the panoramic camera system of Hexagon and Corona, and the mapping camera system of Hexagon (modified from [193]). d) An example of Hexagon mapping camera image (KH-9) with metadata information (modified from [24]) and e) an aft and forward panoramic camera image (KH-4).

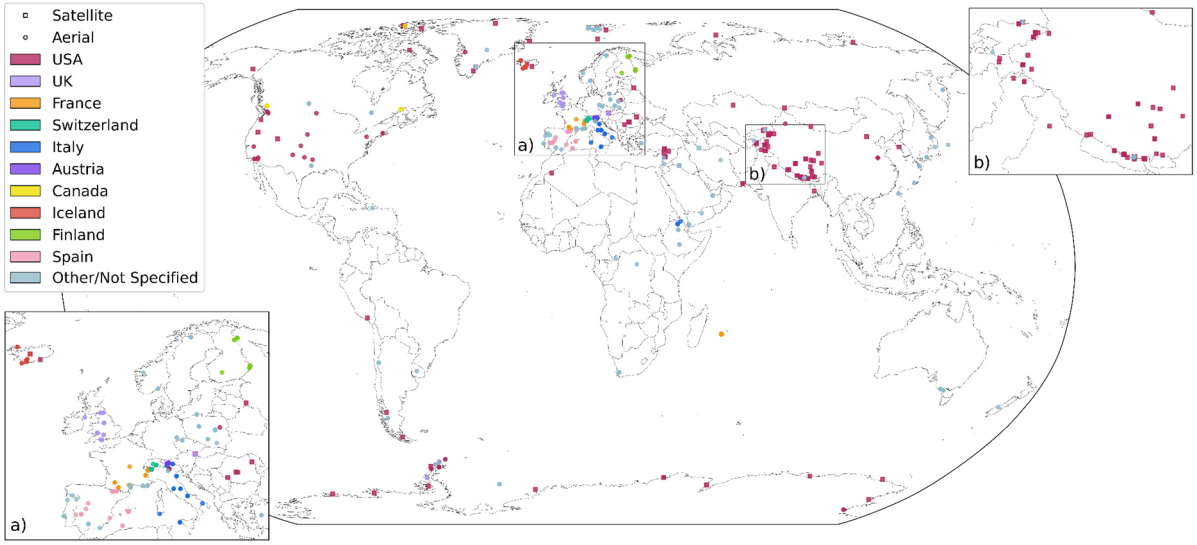

Fig. 4. Spatial distribution of the research study sites coloured by country of aerial and satellite historical image archives.

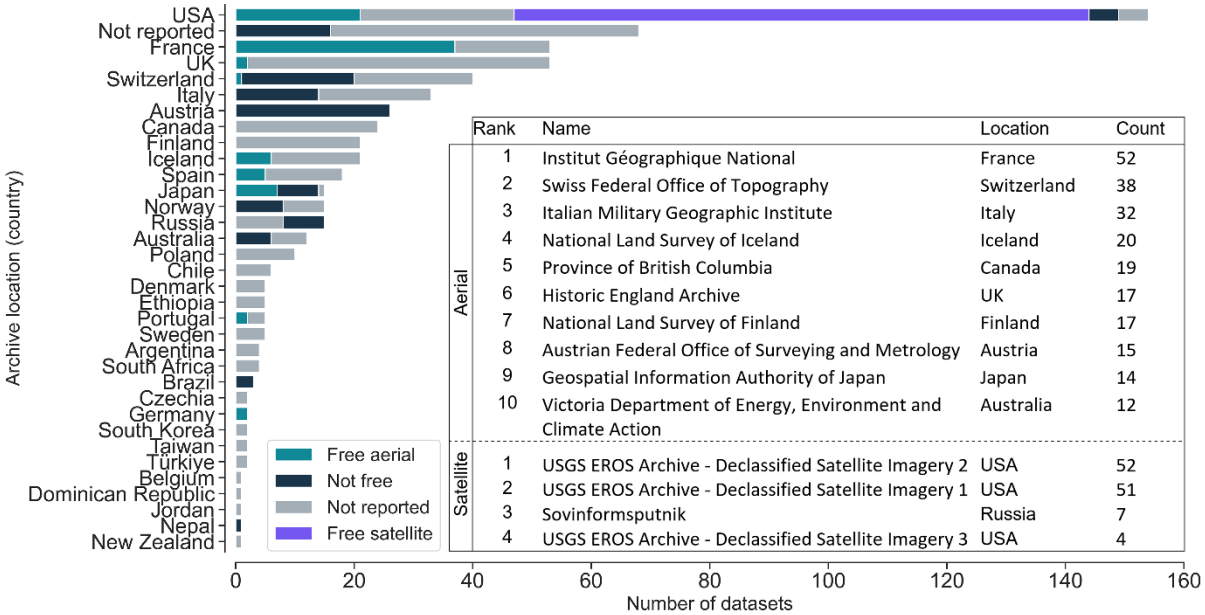

	Rank	Name	Location	Count
Aerial	1	Institut Géographique National	France	52
	2	Swiss Federal Office of Topography	Switzerland	38
	3	Italian Military Geographic Institute	Italy	32
	4	National Land Survey of Iceland	Iceland	20
	5	Province of British Columbia	Canada	19
	6	Historic England Archive	UK	17
	7	National Land Survey of Finland	Finland	17
	8	Austrian Federal Office of Surveying and Metrology	Austria	15
	9	Geospatial Information Authority of Japan	Japan	14
	10	Victoria Department of Energy, Environment and Climate Action	Australia	12
Satellite	1	USGS EROS Archive - Declassified Satellite Imagery 2	USA	52
	2	USGS EROS Archive - Declassified Satellite Imagery 1	USA	51
	3	Sovinformsputnik	Russia	7
	4	USGS EROS Archive - Declassified Satellite Imagery 3	USA	4

Fig. 5. Country of aerial and satellite image archives and the number of processed datasets per archive location, coloured by their availability: freely or not freely available and not reported. The spy satellite archive is only in the USA and Russia ("Not free"). Archive countries with 1 dataset are sorted alphabetically based on country name. The table lists the top ten most accessed aerial image archives in the review studies. Of spy satellites, only four separate archives were accessed in the USA and Russia.

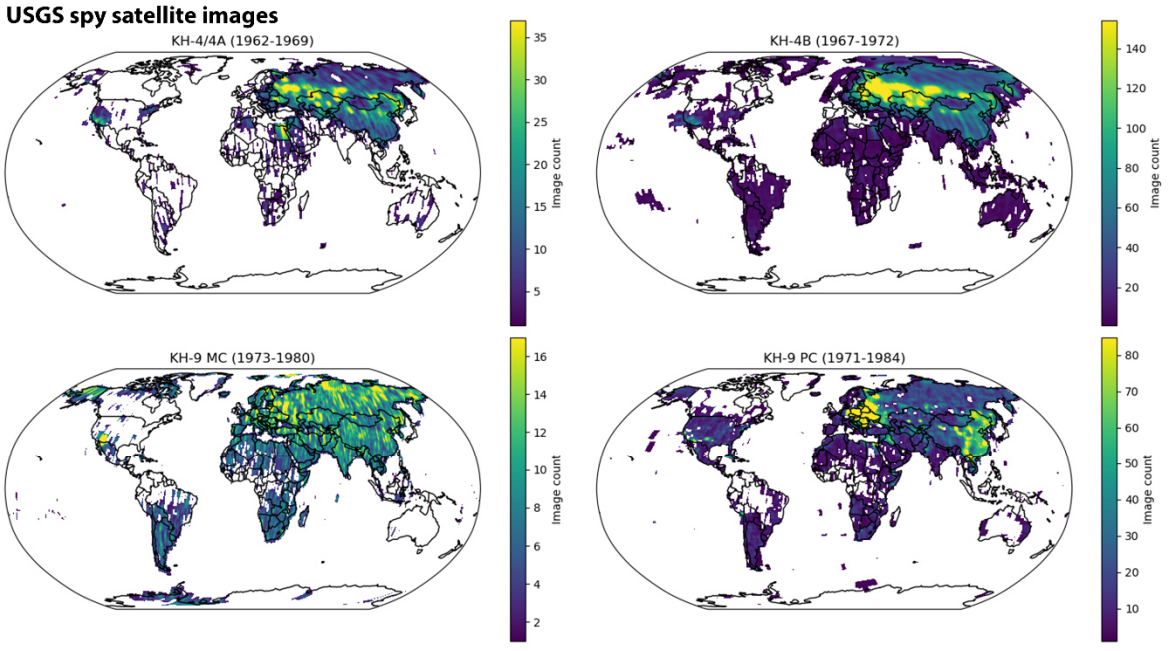

(a)

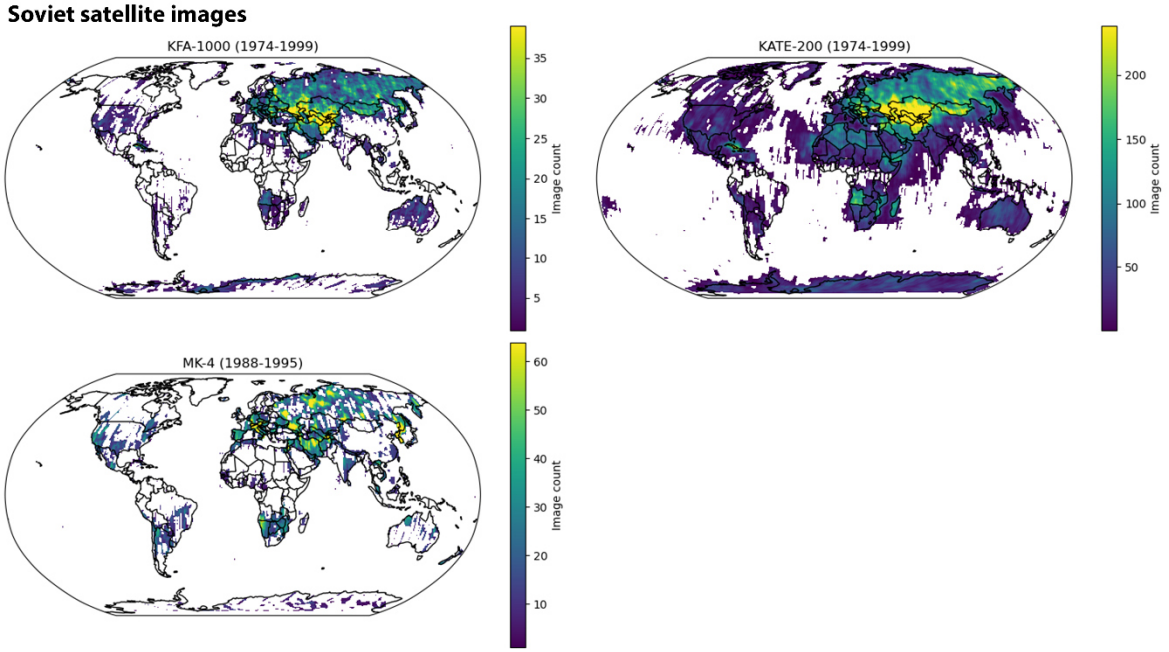

(b)

Fig. 6. Coverage of satellite images in the a) USGS Declass (image footprints courtesy of the USGS) and b) Soviet satellite archives with stereoscopic ability (image footprints courtesy of Anders Anker Bjørk).

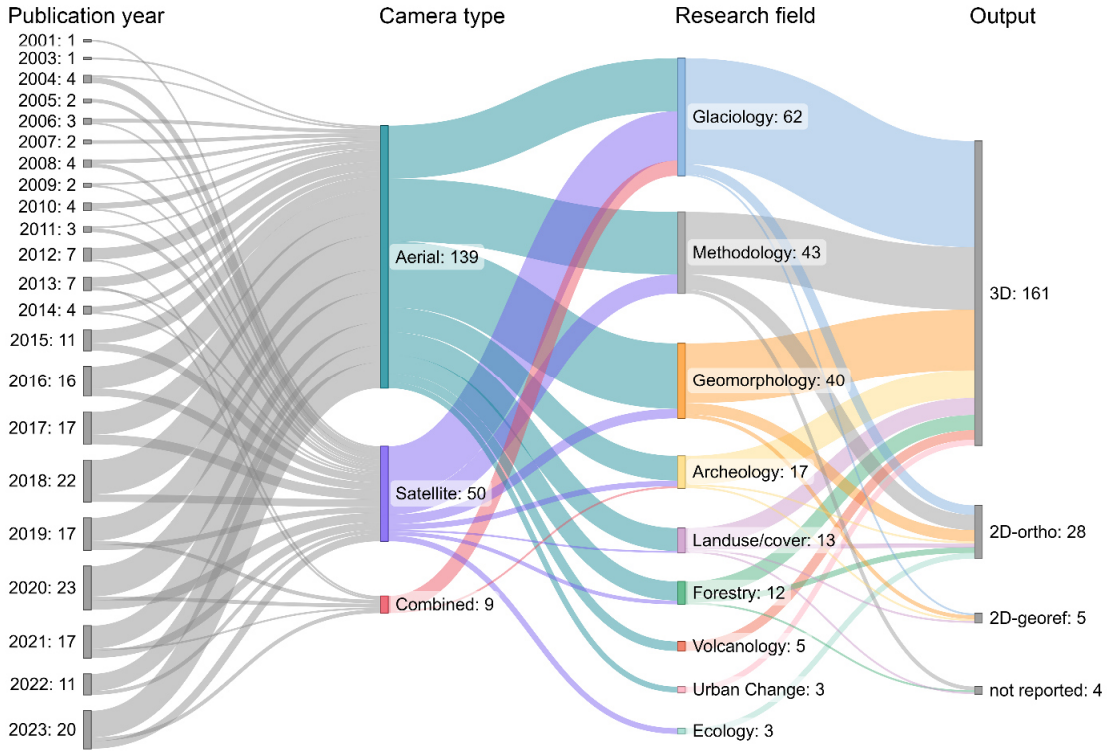

Fig. 7. Database visualisation based on 198 reviewed studies. The output product is "3D", i.e. point cloud and/or DEM, "2D-ortho", i.e. only orthoimages were generated, "2D-georef" where the focus was on georeferencing solutions, "Combined" are studies that used both aerial and satellite images, and "not reported" when not indicated in the study. The figure was produced with SankeyMATIC [194].

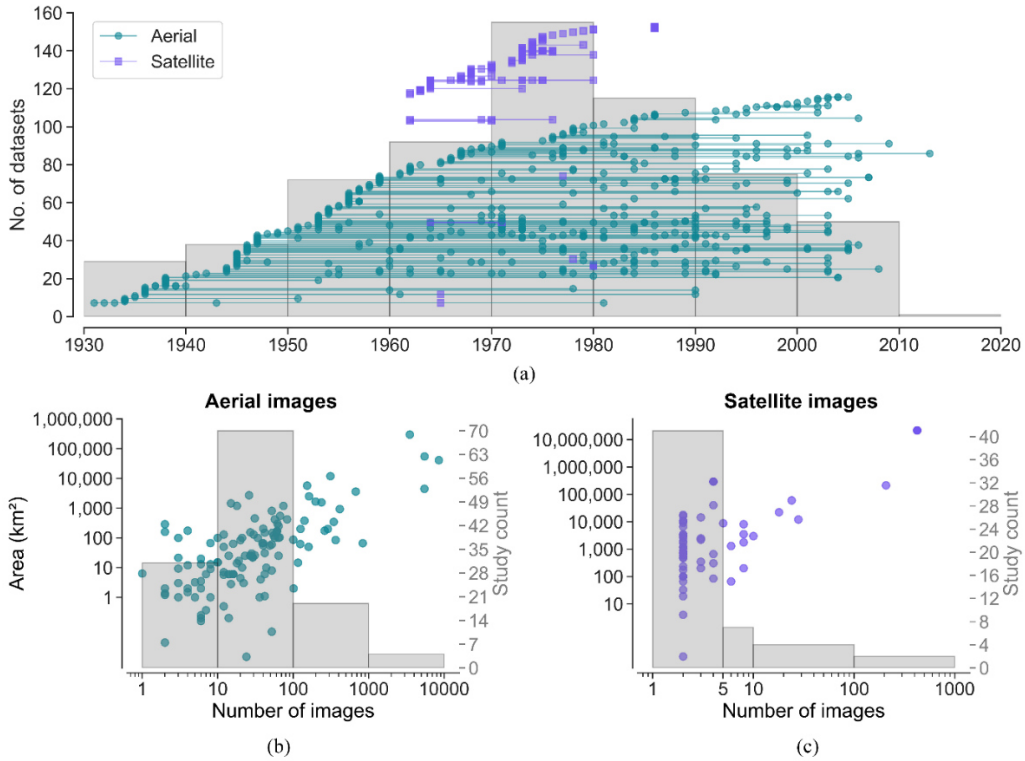

Fig. 8. a) The timeline of processed historical image datasets for each study, with a histogram of the datasets processed from each decade. The considered 198 studies contained a total of 630 datasets. Markers connected by a horizontal line indicate individual datasets for the same study, sorted by data type and year of image acquisition. The number of processed b) aerial and c) spy satellite images and the corresponding reconstructed area in square km for each study. The axes are in a logarithmic scale. Note that 144 aerial datasets from 28 studies and 10 satellite datasets from 6 studies did not report the number of images.

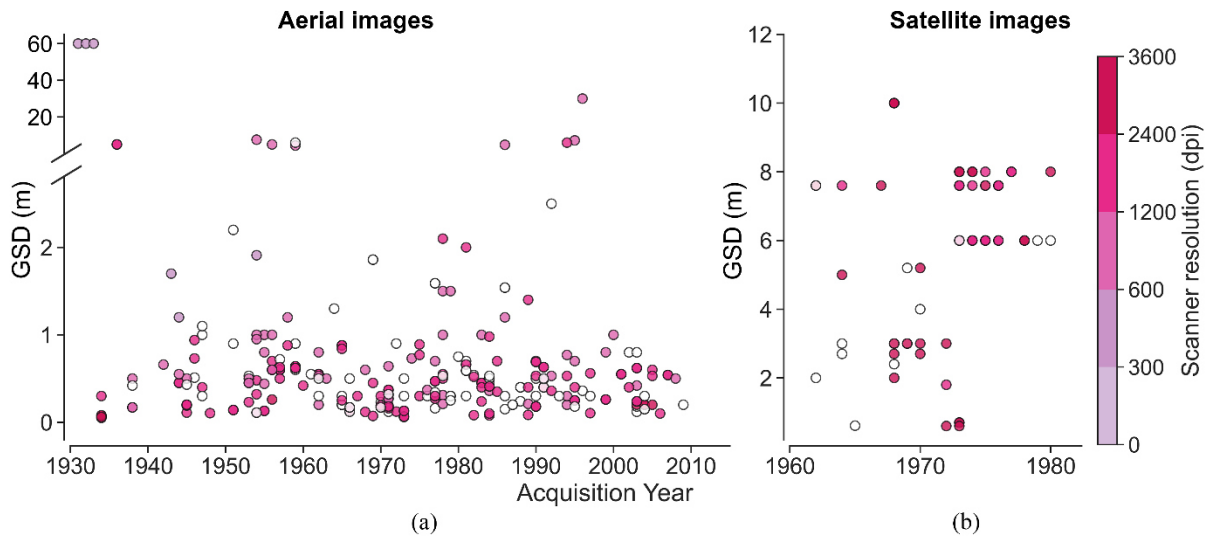

Fig. 9. The Ground Sampling Distance (GSD) of a) aerial and b) spy satellite image datasets coloured by scanning resolution in dpi. White dots indicate that the scanner resolution was not reported.

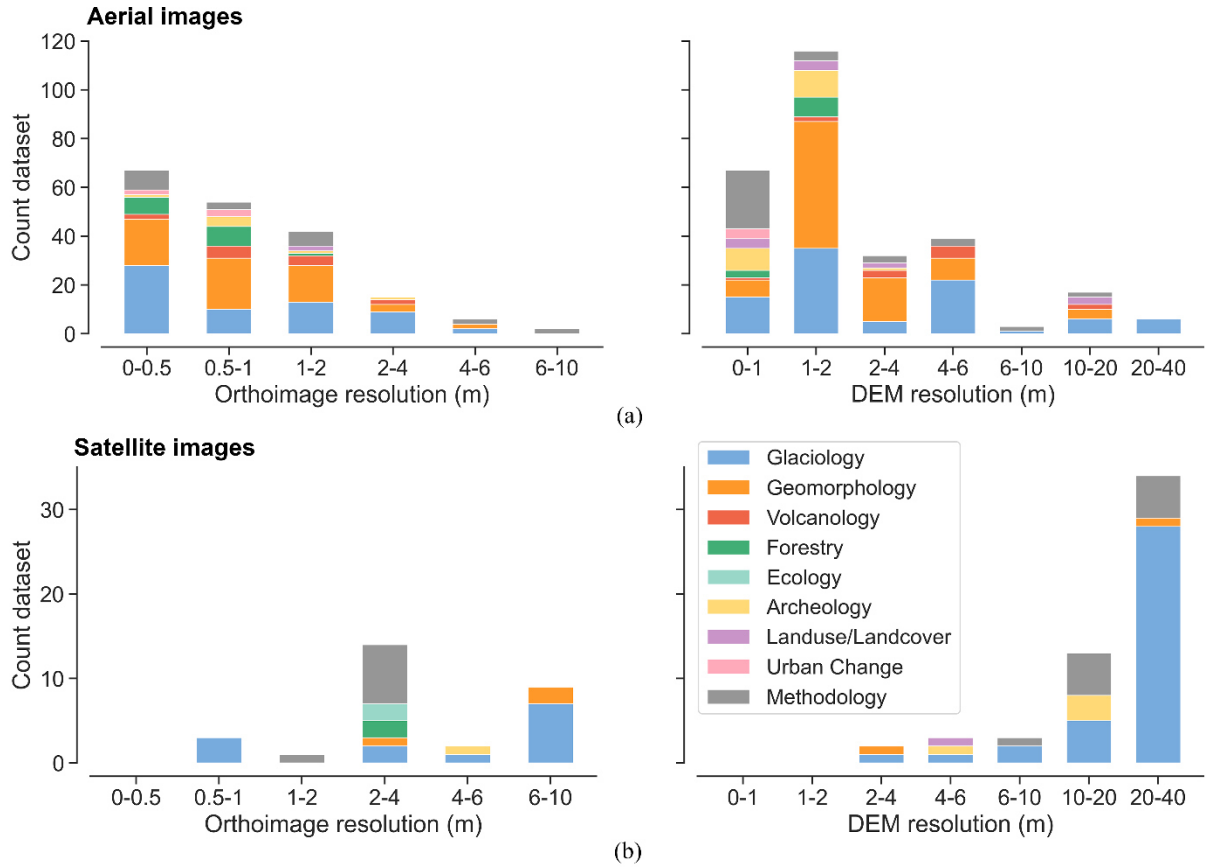

Fig. 10. Resolution of the orthophotos generated from a) aerial images and c) satellite images, and the resolution of DEMs generated from b) aerial images and d) satellite images.

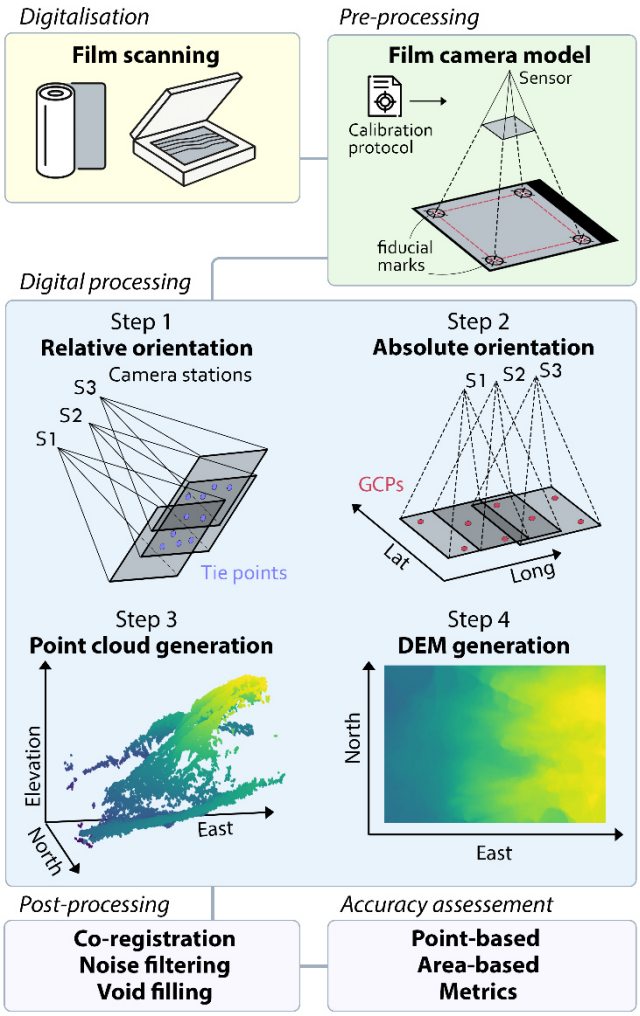

Fig. 11. Graphic illustration of digital processing of historical stereo images from film scanning to post-processing.

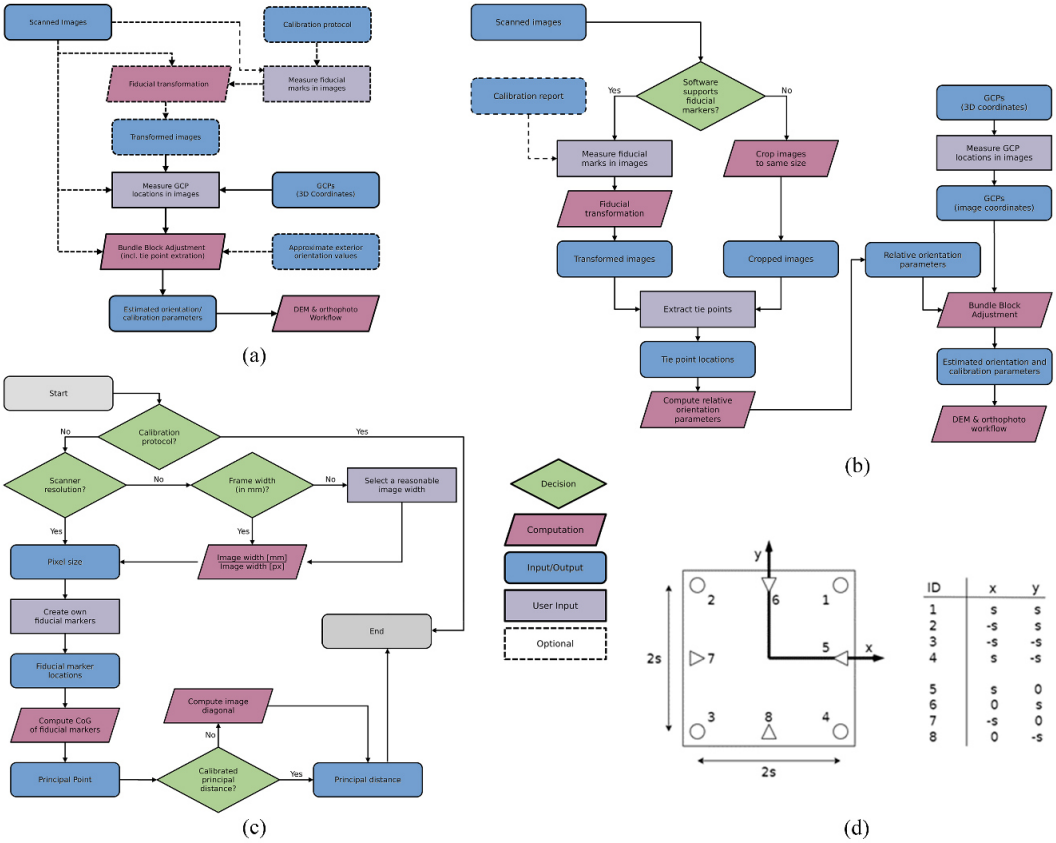

Fig. 12. Historical images data processing workflow. a) General photogrammetric workflow. b) SfM workflow for Image Orientation. c) Workflow for obtaining interior orientation parameters in case of missing calibration protocol.

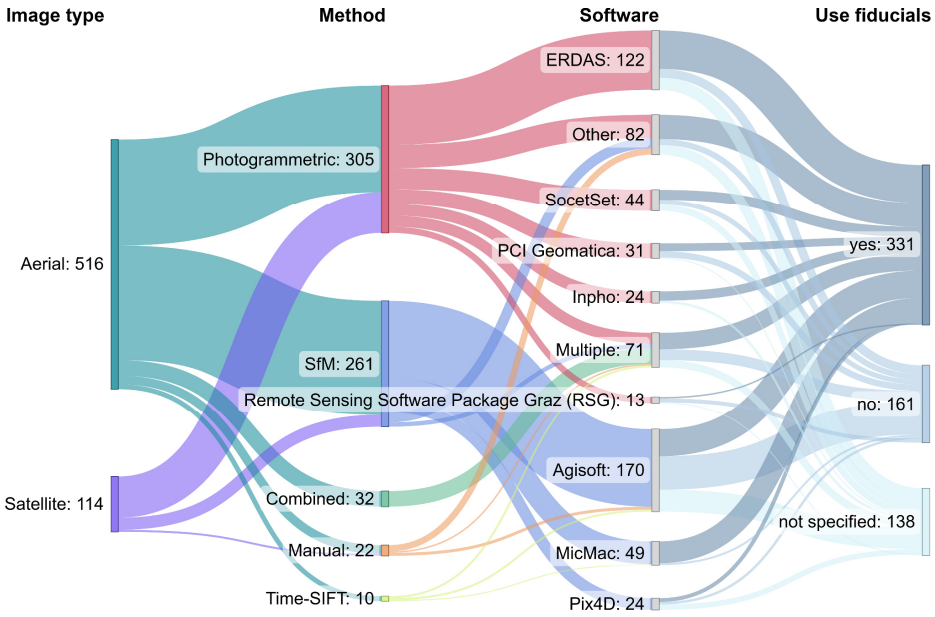

Fig. 13. Distribution of the processing methods, software, and use of the fiducial mark for aerial and spy satellite historical image studies. “Combined” methods include studies that use Photogrammetric and SfM solutions, while “Multiple” software indicates that multiple software packages were used for processing. Software that was outside of the top ten is reclassified as “Other”, consisting of the following: 2OC, Ames Stereo Pipeline, ArcGIS Pro, BLUH, CoSP, ENVI, ESPA, GRAPHOS, Geomatica Banff, HEXIMAP, OpenDroneMap, PhoTopol, PhotoMod, SAPC, SURE, VirtuoZo, Z-Space, Z/I Imaging: ISAE, self-implemented algorithms (9 datasets), or not reported (19 datasets). The figure was produced with SankeyMATIC [194].

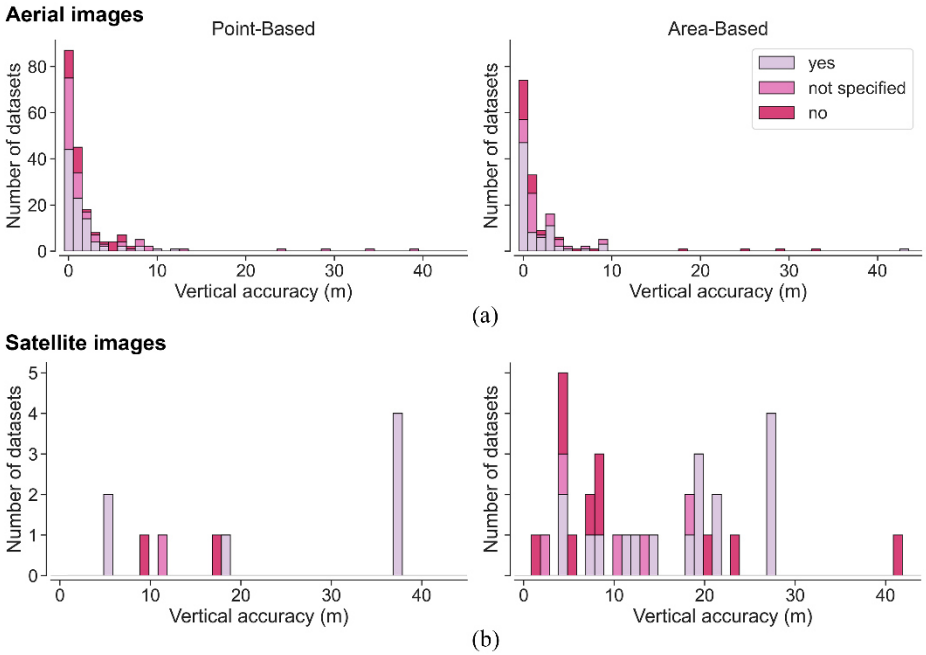

Fig. 14. Vertical accuracy (RMSE and standard deviation) in metres of a) aerial images and b) satellite images, based on their comparison with reference data grouped as point-based or area-based. Colours indicate the usage of fiducial marks in the processing.

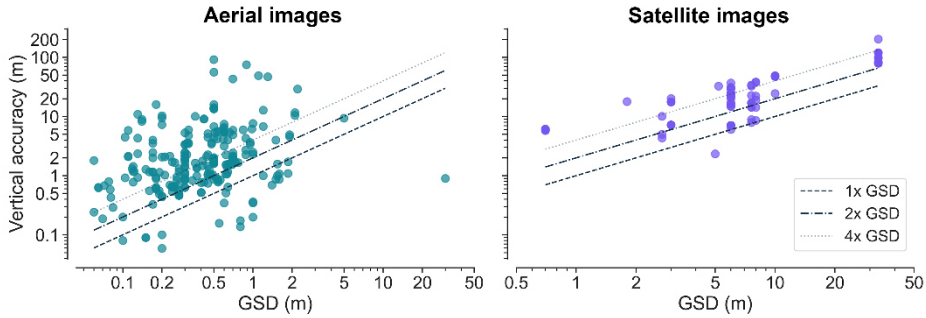

Fig. 15. Reported accuracy in metres (RMSE and standard deviation) compared to reference datasets in relation to the Ground Sampling Distance (GSD) of processed aerial and satellite images.

Table 1. Factors that impact the image quality and digital photogrammetric processing of historical aerial and satellite images. Each factor introduces specific technical challenges that limit the generation of accurate 3D reconstructions and orthoimages from historical imagery.

Factor category	Description	Challenges in photogrammetric processing
Image acquisition and type	Camera quality (metric vs. non-metric) and type (oblique/panoramic image), focal length, flight height, low image overlap, poor focus	Heterogeneity on image scale/size, tie-point matching issues, gaps in DEM and orthoimage, geometric distortions
Acquisition time and surface	Illumination conditions, clouds, image saturation, surface change between acquisitions, low texture and contrast	Poor feature extraction, fewer tie-points, low accuracy in camera orientation and 3D reconstruction, gaps in DEM and orthoimage
Image digitisation	Scanner type and settings, scanning resolution, inconsistent digitisation between images, scanning artefacts and distortions	Reduced image detail, distortions in DEMs, pre-processing required
Metadata availability	Missing or incomplete flight/calibration data, absence of GCPs	Inaccurate orientation, scaling errors, difficulties in bundle adjustment and processing in photogrammetric software
Preservation and storage	Film degradation, discolouration, scratches, shrinking or warping of photo paper	Geometric distortions, non-conformal deformations, reduced photogrammetric accuracy

Table 2. A selection of the institutions and image archives used in the reviewed studies. "Link" is the archive webpage, while "GeoURL" is the link to the geoportal. The USGS EROS archives offer free-of-charge downloads for scanned images; additional scans can be ordered for $30.

Location	Archive or Institution Name	Acronym	Free download	No. images	Start Year	End Year	Link	GeoURL
Argentina	Instituto Geográfico Nacional de Argentina	IGNA	unclear	-	1933	1982	website	-
Argentina	Servicio de Hidrografía Naval Argentino	SHNA	unclear	-	-	-	website	-
Austria	Austrian Federal Office of Surveying and Metrology	BEV	no	450000	1949	2009	website	-
Austria	Office of the Tyrolean Government	OTG	no	-	1946	-	website	website
Belgium	Royal Museum for Central Africa	RMCA	unclear	-	1950	-	website	-
Canada	National Air Photo Library of Natural Resources Canada	NAPL	no	-	-	-	website	-
Canada	Geomatheque Ltd., QC	GeoQC	no	-	1959	-	website	-
Canada	Province of British Columbia	GeoBC	no	2500000	1936	-	website	-
Denmark	Agency for Data Supply and Efficiency	SDFE	unclear	-	-	-	website	-
Denmark	National Danish Survey and Cadastre	KMS	unclear	-	1936	1992	website	website
Ethiopia	Space Science and Geospatial Institute	EMA	unclear	34000	1935	1943	website	-
Finland	Finnish Defence Forces	FDF	no	-	1931	-	website	website
Finland	National Land Survey of Finland	NLS	unclear	-	1930	2008	website	-
France	Institut Géographique National	IGN	yes	-	-	-	website	-
Iceland	National Land Survey of Iceland	LMÍ	yes	140000	1937	2000	website	website
Italy	Italian Military Geographic Institute	IGMI	no	300000	1927	2010	website	website
Japan	Cryosphere Data Archive Partnership Observational Research Database	CrDAP	unclear	-	-	-	website	-
Japan	Geospatial Information Authority of Japan	GIAJ	unclear	-	1946	-	website	-
Norway	Norwegian Mapping Authority	Kartverket	no	1300000	1935	-	website	-
Norway	Norwegian Polar Institute	NPI	no	60000	-	-	website	-
Poland	State Geodetic and Cartographic Resource	Czgik	unclear	-	-	-	website	website
Portugal	Portuguese Army Geography Institute	IGeoE	no	-	1937	2002	website	-
South Africa	National Geo-spatial Information	NGI	unclear	-	1926	2008	website	website
Spain	Cartographic and Geological Institute of Catalonia	ICGC	unclear	1000000	1942	-	website	website
Spain	Institut Cartogràfic Valencià	ICV	unclear	-	-	-	website	website
Spain	Centro Nacional de Información Geográfica	CNIG	yes	-	1929	2007	website	website
Sweden	Swedish mapping, cadastral, and land registration authority	Lantmäteriet	unclear	-	1920	2006	website	-
Switzerland	Swiss Federal Institute of Technology Library 'e-pics' imagery archive	ETHZ	unclear	-	1918	2011	website	website
Switzerland	Swiss Federal Office of Topography	Swisstopo	yes	-	1927	2010	website	website
UK	Agricultural Development and Advisory Service	ADAS	unclear	-	1959	2007	website	-
UK	Historic England Archive	HEA	unclear	400000	-	-	website	-
UK	Royal Commission on the Ancient and Historical Monuments of Wales	RCAHMW	unclear	-	-	-	website	website
UK	Scott Polar Research Institute	SPRI	unclear	100000	-	-	website	-
UK	National Collection of Aerial Photography	NCAP	unclear	-	-	-	website	-
UK	Britain From Above	BFA	unclear	1260000	1919	2006	website	website
UK	University of Cambridge Committee for Aerial Photography	CUCAP	no	500000	1947	-	website	-
UK	British Antarctic Survey	BAS	no	-	1936	2005	website	website
USA	Arctic Data Center	ADC	unclear	-	-	-	website	-
USA	Connecticut State Library	CSL	unclear	-	-	-	website	website
USA	Texas Data Repository (Historical Air Photo Dataverse)	TxGIO	no	1000000	1920	-	website	website
USA	University of California, Riverside	UCR	unclear	-	1938	2000	website	website
USA	USGS EROS - Aerial Photography - Air Photo Single Frames	USGSAF	yes	5950000	1937	2014	website	website
USA	USGS EROS - Aerial Photography - Antarctic Single Frame Records	USGSAnt	yes	375000	1946	2000	website	website
USA	USGS EROS - Declassified Satellite Imagery 1	Declass1	yes	840000	1960	1972	website	website
USA	USGS EROS - Declassified Satellite Imagery 2	Declass2	yes	47000	1963	1980	website	website
USA	USGS EROS - Declassified Satellite Imagery 3	Declass3	yes	600000	1971	1984	website	website
USA	USGS EROS - National Aerial Photography Program	NAPP	yes	1300000	1987	2007	website	website
USA	USGS EROS - National High Altitude Photography	NHAP	yes	500000	1980	1989	website	website
USA	USGS North American Glacier Aerial Photography	NAGAP	yes	-	1964	1997	website	-
USA	US National Archives Cartographic and Architectural Branch	NARA	no	35000000	1918	2011	website	-

Table 3. Main characteristics of the American stereo reconnaissance programme. NRO is the National Reconnaissance Office. Acquisition height is approximately 160 km for all missions, and scanning resolution is 7 µm for USGS data.

Series	**Corona**			**Gambit**		**Hexagon**	
Spacecraft	KH-4	KH-4A	KH-4B	KH-7	KH-8	KH-9	KH-9
Period of operation	1962-1963	1963-1969	1967-1972	1963-1967	1966-1982	1971-1984	1973-1980
Camera name	M	J-1	J-3	Gambit-strip	Gambit-strip	Panoramic camera	Mapping camera
Camera type	Panoramic			Strip	Strip	Panoramic	Frame
Focal length (mm)	609.6	609.6	609.6	4445	4445	1500	304.8
Highest ground resolution (m)	3.6	2.7	1.8	0.6	0.6	0.6	6
Film format (cm)	7 x 80	7 x 80	7 x 80	24 x variable	12.7 x variable	15 x variable	23 x 46
Fiducial marks	no	no	no	yes	yes	yes	yes
References	NRO (1970)	NRO (1970)	NRO (1967)	Burnett (1982)	Burnett (1982)	NRO (1969)	Burnett (1982)

Table 4. Main characteristics of the Soviet stereo reconnaissance programme.

Series	**Zenit**													**Yantar**			
Spacecraft	Zenit-2/ -2M/ NKh		Zenit-4/ -4M/ -4MK/ -4MKM/ -4MKT/ -4MT			Zenit-6	Zenit-8			Resurs-F1/ -F1M		Resurs-F2	Resurs-F3	1KFT		2K	4K1/ 4K2/ 4K2M
Period of operation	1961-1979		1963-1985		1971-1982	1976-1984	1984-1994	1979-1999		1987-1995	1989-1994	1963-1967	1966-1982	1981-2005		1974-1983	1979-2015
Altitude (km)	~200					207	215	200		189	175	~200		200		170	
Max duration (days)	14					15	25	23		30	20	14		45		30	180
Camera name	SA-20 (1-3)	SA-10 (1)	KFA-1000 (1)	KATE-200 (1-5)	TK-250 (1)	–	KFA-3000 (2)	KFA-1000 (2)	KATE-200 (3)	MK-4 (4)	KFA-3000 (2)	SA-20 (1-3)	SA-10 (1)	TK-350 (1)	KVR-1000 (1)	Zhemchug-4	Zhemchug-18
Camera type	Frame	Frame	Frame	Frame	Frame	–	Frame	Frame	Frame	Frame	Frame	Frame	Frame	Frame	Panoramic	Frame	–
Focal length (mm)	1000	200	1000	200	250	–	3000	1000	200	300	3000	1000	200	350	1000	3000-4000	–
Highest ground resolution (m)	5	25	5	15	20	–	2	5	15	6	2	5	25	8	3	0.5	1.2
Film format (cm)	30x30	18x18	30x30	18x18	30x30	–	30x30	30x30	18x18	18x18	30x30	30x30	18x18	30x45	18x72	30x30	–
Fiducial marks	–	–	yes	yes	yes (reseau)	–	–	yes	yes	yes	–	–	–	yes	yes	–	–
Number missions	182		65		23	97	102	54		10	5	182		21		30	103
Total frame number	–	–	66,686		–	–	–	166,000	206,000	66,686	–	–	–	–	–	–	–